Multiscale Aspects of the 26–27 April 2011 Tornado Outbreak. Part II: Environmental Modifications and Upscale Feedbacks Arising from Latent Processes

MANDA B. CHASTEEN[a,b,c] AND STEVEN E. KOCH[c]

[a] *Cooperative Institute for Mesoscale Meteorological Studies, University of Oklahoma, Norman, Oklahoma*
[b] *School of Meteorology, University of Oklahoma, Norman, Oklahoma*
[c] *NOAA/OAR/National Severe Storms Laboratory, Norman, Oklahoma*

(Manuscript received 2 March 2021, in final form 23 September 2021)

ABSTRACT: One of the most prolific tornado outbreaks ever documented occurred on 26–27 April 2011 and comprised three successive episodes of tornadic convection that culminated with the development of numerous long-track, violent tornadoes over the southeastern United States during the afternoon of 27 April. This notorious afternoon supercell outbreak was preceded by two quasi-linear convective systems (hereinafter QLCS1 and QLCS2), the first of which was an anomalously severe nocturnal system that rapidly grew upscale during the previous evening. Here in Part II, we use a series of RUC 1-h forecasts and output from convection-permitting WRF-ARW simulations configured both with and without latent heat release to investigate how environmental modifications and upscale feedbacks produced by the two QLCSs contributed to the evolution and exceptional severity of this multiepisode outbreak. QLCS1 was primarily responsible for amplifying the large-scale flow pattern, inducing two upper-level jet streaks, and promoting secondary surface cyclogenesis downstream from the primary baroclinic system. Upper-level divergence markedly increased after QLCS1 developed, which yielded strong isallobaric forcing that rapidly strengthened the low-level jet (LLJ) and vertical wind shear over the warm sector and contributed to the system's upscale growth and notable severity. Moreover, QLCS2 modified the mesoscale environment prior to the supercell outbreak by promoting the downstream formation of a pronounced upper-level jet streak, altering the midlevel jet structure, and furthering the development of a highly ageostrophic LLJ over the Southeast. Collectively, the flow modifications produced by both QLCSs contributed to the notably favorable shear profiles present during the afternoon supercell outbreak.

SIGNIFICANCE STATEMENT: The tornado outbreak that impacted the United States on 26–27 April 2011 was part of an extended outbreak that produced 343 tornadoes and numerous fatalities. This paper is Part II of a study that describes the meteorological factors supporting such a prolific event. Herein we investigate the convectively forced environmental modifications that occurred during a 36-h period encompassing three successive convective episodes. The first two episodes collectively altered the upper-level flow pattern and markedly enhanced low-level winds throughout the warm sector. These modifications served as upscale feedbacks that contributed to the first episode's exceptional severity and to the remarkable vertical shear profiles that supported numerous long-track and violent tornadoes during the final episode on the afternoon of 27 April.

KEYWORDS: Ageostrophic circulations; Convection; Convective adjustment; Convective storms/systems; Deep convection; Dynamics; Mesoscale processes; Mesoscale systems; Potential vorticity; Diabatic heating; Extreme events; Jets; Severe storms; Squall lines; Storm environments; Synoptic-scale processes

1. Introduction

In the first part of this study (Chasteen and Koch 2021, hereinafter Part I), we documented how the multiscale environment evolved throughout the 25–28 April 2011 extended tornado outbreak. Particular emphasis was given to the ~36-h period encompassing the lifetimes of three successive tornadic episodes that impacted the southeastern United States on 27 April, including two quasi-linear convective systems (hereinafter QLCS1 and QLCS2) and the notoriously prolific afternoon supercell outbreak (Fig. 1; Knupp et al. 2014). This multiday outbreak occurred ahead of a highly amplified and slowly moving upper-level trough as three embedded shortwaves supported destabilization and episodic convective development over the south-central United States. The formation of QLCS1 on the evening of 26 April was immediately followed by dramatic and sustained changes to the upper-level flow pattern and concomitant strengthening of the low-level flow and vertical wind shear throughout the warm sector. QLCS1 intensified as it rapidly grew upscale overnight, and we hypothesized that—through producing these upscale environmental modifications—the system was able to enhance its own severity. Furthermore, the subsequent formation of QLCS2 was accompanied by changes to the midlevel jet structure and further strengthening of the low-level flow that ultimately contributed to the remarkable shear profiles present over the Southeast at the beginning of the supercell outbreak.

Highly amplified and slowly moving synoptic patterns are common during tornadic events in the Southeast (e.g., Galway and Pearson 1981; Guyer et al. 2006; Sherburn et al. 2016)

Koch: Retired.

Corresponding author: Manda B. Chasteen, manda.chasteen@ou.edu

DOI: 10.1175/MWR-D-21-0014.1

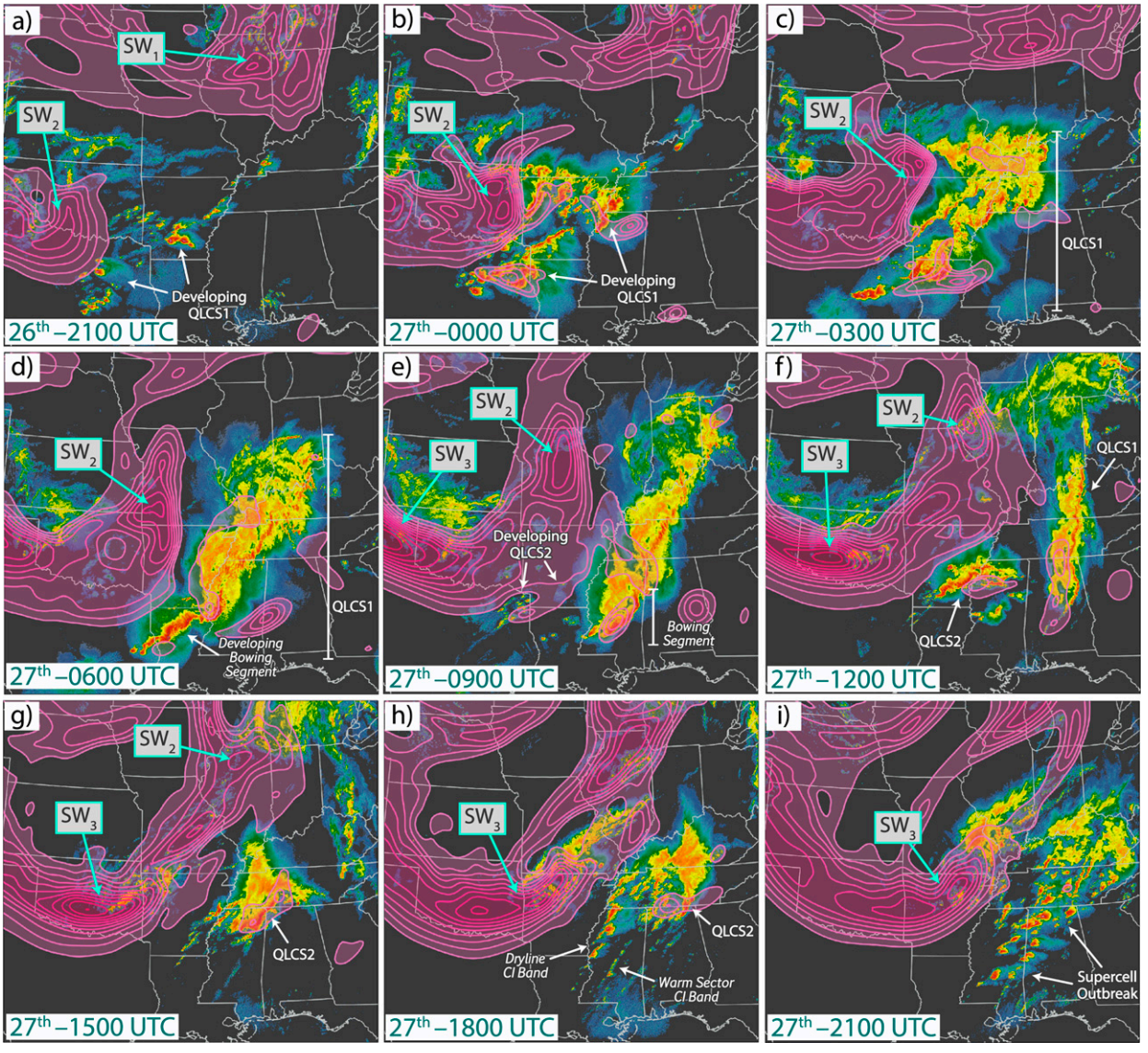

FIG. 1. NEXRAD composite radar reflectivity overlaid with PV averaged in the 400–300-hPa layer (pink contours; every 0.5 PVU ≥ 1 PVU) from the corresponding RUC 1-h forecast valid at (a) 2100 UTC 26 Apr, (b) 0000 UTC 27 Apr, (c) 0300 UTC 27 Apr, (d) 0600 UTC 27 Apr, (e) 0900 UTC 27 Apr, (f) 1200 UTC 27 Apr, (g) 1500 UTC 27 Apr, (h) 1800 UTC 27 Apr, and (i) 2100 UTC 27 Apr 2011.

and – in general – often support prolonged periods of active convection (e.g., Stensrud 1996; Hamill et al. 2005). Sustained interactions between mesoscale regions of latent heating and a strongly baroclinic environment may induce considerable upscale flow modifications that ultimately act as feedbacks to enhance the severity and persistence of ongoing or subsequent convection. This may occur through upper-level alterations that enhance forcing for ascent near the convection and/or through low-level jet (LLJ) intensification, which yields stronger vertical wind shear, poleward moisture transport, and moisture convergence (e.g., Ninomiya 1971; Keyser and Johnson 1984; Wolf and Johnson 1995; Lackmann 2002). Such modifications often compound during multiepisode convective events. Stensrud (1996) found that multiple convective systems occurring over 2–3 days collectively amplified the large-scale flow pattern, strengthened the LLJ, and increased poleward moisture transport throughout the warm sector—favorable conditions for subsequent convective development. Furthermore, Trapp (2014) found that tornado outbreaks often culminate following multiday periods of severe weather and hypothesized that this tendency may be attributable to upscale feedbacks produced by convection during the previous days.

Because of the established difficulty in accurately predicting convective events in the Southeast (e.g., Dean and Schneider 2008; Rasmussen 2015) and the general predictability challenges inherent in forecasting individual convective episodes (e.g., Zhang et al. 2007; Melhauser and Zhang 2012; Weisman et al. 2015), an evaluation of the scale interactions and upscale

feedbacks that occur during multiepisode severe outbreaks in the Southeast is warranted. Expanding upon the findings of Part I, this Part II provides a detailed dynamical investigation into the upscale environmental modifications produced by QLCS1 and QLCS2 and how they contributed to the overall outbreak severity and evolution. Using environmental fields from the RUC model and convection-permitting WRF-ARW simulations configured with and without latent heating, we demonstrate that the QLCSs collectively altered the environment on multiple scales prior to the afternoon supercell outbreak. The remainder of this paper is organized as follows. Section 2 provides an overview of the RUC model. Section 3 reviews the outbreak evolution described in Part I. The upscale environmental modifications produced by the QLCSs are detailed in section 4 using the RUC fields and investigated further in section 5 using the WRF simulations. Section 6 provides a summary and discussion of our primary findings.

2. RUC 1-h forecasts

Environmental analyses were conducted using a series of 1-h forecasts from the NOAA/NCEP operational RUC hourly assimilation system and mesoscale forecast model (Benjamin et al. 2004a,b). The RUC used a diabatic digital filter initialization technique to mitigate model imbalance induced through the assimilation procedure. Thus, forecasts valid 1 h after model initialization are known to retain accuracy while exhibiting greater stability and less noise than the 0-h analyses (Benjamin et al. 2004b), justifying their use herein as we investigate regions of dynamical imbalance. The RUC model had a 13-km horizontal grid spacing, and convection was represented implicitly via a cumulus parameterization (i.e., internal convective-scale circulations were not directly resolved).

3. Review of the 26–27 April 2011 outbreak evolution

We first recap the primary findings of Part I, wherein we described the environmental evolution that supported three tornadic episodes on 26–27 April 2011. As previously mentioned, the extended outbreak occurred ahead of a slowly moving longwave trough and pronounced upper-level jet streak "J_1" as three embedded shortwaves (hereinafter "SW_1," "SW_2," and "SW_3") sequentially moved into the south-central United States (Figs. 1 and 2). The first shortwave SW_1 emerged on 25 April and amplified considerably with time over the Midwest, promoting the development of a "PV hook" structure (characteristic of Rossby wave breaking; Thorncroft et al. 1993), the eastward expansion of the longwave trough, and the occlusion of a surface low (i.e., "L_1") over Wisconsin by 2100 UTC 26 April, when QLCS1 was beginning to form ahead of SW_2 (Figs. 2a and 3a).

Convection initiation (CI) associated with QLCS1 largely occurred ahead of the dryline in eastern Texas and along and north of an effective warm front[1] over Arkansas (Fig. 1a). This widespread convection congealed into an expansive and notably tornadic QLCS that progressed through the warm sector ahead of SW_2 (Figs. 1b–f). This evolution was accompanied by the rapid formation and poleward advancement of a prominent jet streak "J_2" immediately after CI, upper-level ridge amplification over the Midwest, and the subsequent development of "J_3" behind QLCS1 (Figs. 2b–d). Furthermore, the LLJ considerably strengthened overnight ahead of QLCS1 as the system grew upscale and intensified, while surface cyclogenesis (i.e., "L_2") had commenced over the Midwest ahead of SW_2 by 1200 UTC 27 April.

The primary shortwave SW_3 associated with J_1 progressed into the southern Great Plains (SGP) early on 27 April and promoted the gradual baroclinic redevelopment of a lee cyclone into "L_3," the movement of a Pacific cold front into Texas, and the resultant formation of a cold front aloft (CFA). Elevated convection associated with QLCS2 developed at ~0900 UTC 27 April as the environment in the wake of QLCS1 destabilized ahead of SW_3 (Fig. 1e). This system's upscale growth into a bow echo was accompanied by the formation of a prominent jet streak "J_4" over the Midwest and further intensification of the LLJ over the Southeast during the morning (Figs. 2c,d). Although QLCS2 became increasingly disorganized prior to the supercell outbreak, residual precipitation and cloud cover associated with the system sustained a thermal boundary—which behaved as an effective warm front—over northern Mississippi and Alabama throughout the afternoon.

Finally, the afternoon supercell outbreak commenced over the Southeast as SW_3, its attendant deep tropopause fold (hereinafter "primary tropopause fold"), and L_3 progressed into Arkansas (Figs. 1h,i). A strong LLJ had become established over the region following the accumulated flow intensification that began during the previous evening (Figs. 2d–f), while midlevel winds strengthened to the south of QLCS2 throughout the morning in association with the approaching J_1. Accordingly, the preconvective environment was characterized by appreciable vertical wind shear and storm-relative helicity (SRH; Davies-Jones 1984), which was paired with anomalously high CAPE to yield conditions incredibly conducive to long-lived supercells and violent tornadoes. Organized CI primarily occurred after 1800 UTC 27 April along two bands: 1) the dryline, which resulted from diurnal modifications to postfrontal air, and 2) the CFA, which advanced over the warm sector ahead of the dryline (Figs. 1h). The resultant supercells remained largely discrete for several hours as they moved through the warm sector, enabling the sheer severity of this final tornadic episode.

4. Environmental modifications and scale interactions

a. Background

Various environmental modifications stemming from convection have been documented in the literature. These include the development of pressure perturbations and resultant (unbalanced) divergent secondary circulations comprising upper-level outflow, low-level inflow, and compensating subsidence and the environmental adjustments that occur via the

[1] The term *effective warm front* designates boundaries at the periphery of the warm sector that was undisturbed by previous convection (Part I).

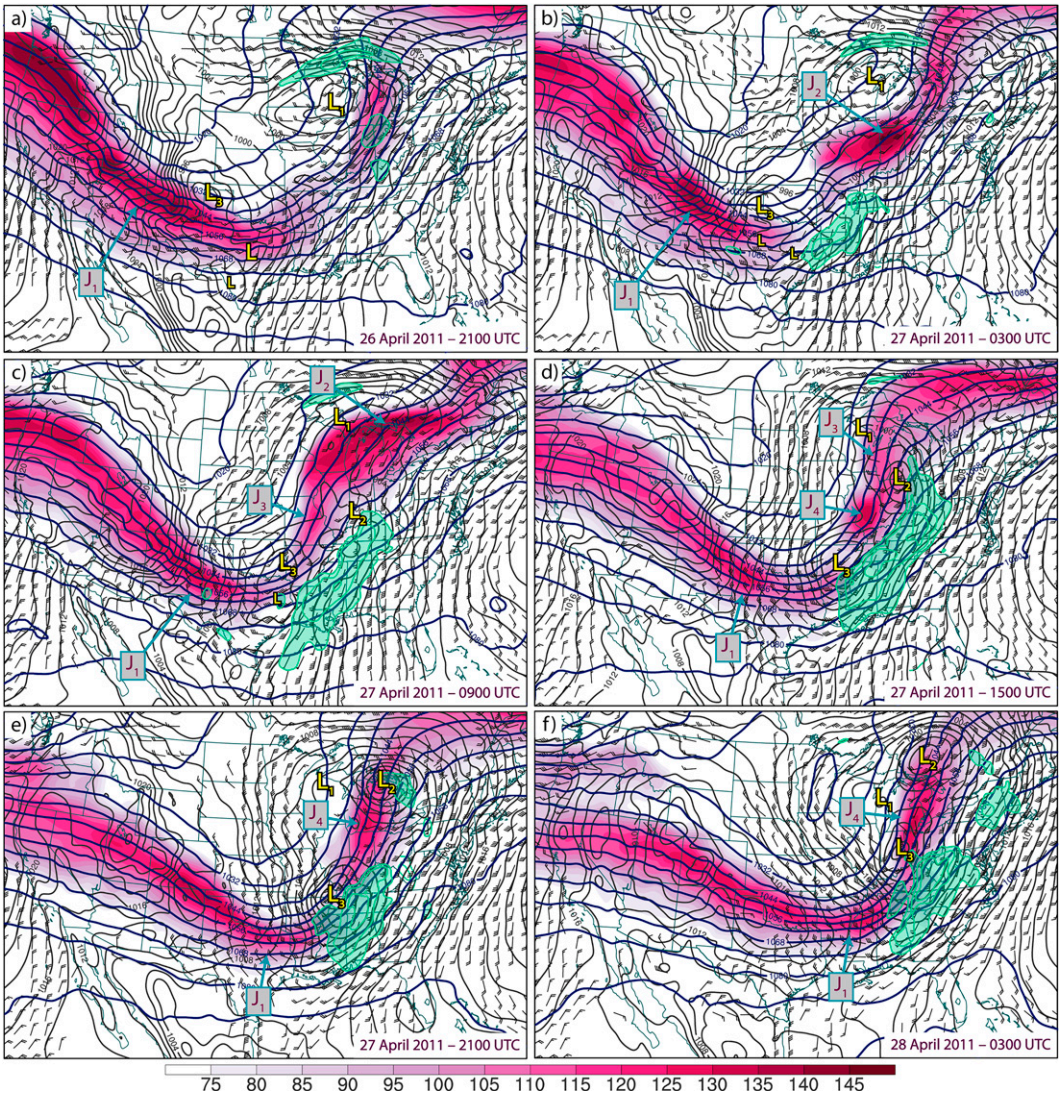

FIG. 2. The 250-hPa wind speed (pink shading; kt), 250-hPa geopotential height (blue contours; dam), SLP (gray contours; hPa), 850-hPa winds (barbs; kt), and 850-hPa wind speed (green shading > 50 kt, with contours every 10 kt ≥ 50 kt) from the corresponding RUC 1-h forecast valid at (a) 2100 UTC 26 Apr, (b) 0300 UTC 27 Apr, (c) 0900 UTC 27 Apr, (d) 1500 UTC 27 Apr, (e) 2100 UTC 27 Apr, and (f) 0300 UTC 28 Apr 2011. Low pressure centers are denoted by a yellow "L."

outward propagation of low-frequency gravity waves (e.g., Bretherton and Smolarkiewicz 1989; Nicholls et al. 1991; Olsson and Cotton 1997; Lane and Reeder 2001). As convection grows upscale into a large mesoscale convective system (MCS), geostrophic adjustment promotes the gradual transition (over ~3–6 h at midlatitudes) toward rotational (balanced) circulations that include a negative PV anomaly and perturbation anticyclone in the upper troposphere—above the level of maximum heating—and a positive PV anomaly and perturbation cyclone (i.e., a mesoscale convective vortex; MCV) in the middle to lower troposphere—below the level of maximum heating (e.g., Maddox 1980; Fritsch and Maddox 1981; Cotton et al. 1989; Davis and Weisman 1994; Olsson and Cotton 1997).

The height and wind perturbations accompanying MCSs are often large and may promote considerable upscale flow modifications and jetogenesis—particularly downstream from the system at upper levels (i.e., an outflow jet) and along its flanks where the background height gradient becomes amplified (e.g., Ninomiya 1971; Maddox et al. 1981; Anthes et al. 1982; Wetzel et al. 1983; Keyser and Johnson 1984; Wolf and Johnson 1995; Rowe and Hitchman 2016). Furthermore, MCSs may influence surface cyclogenesis—both through diabatic amplification and enhancing the background baroclinity—a

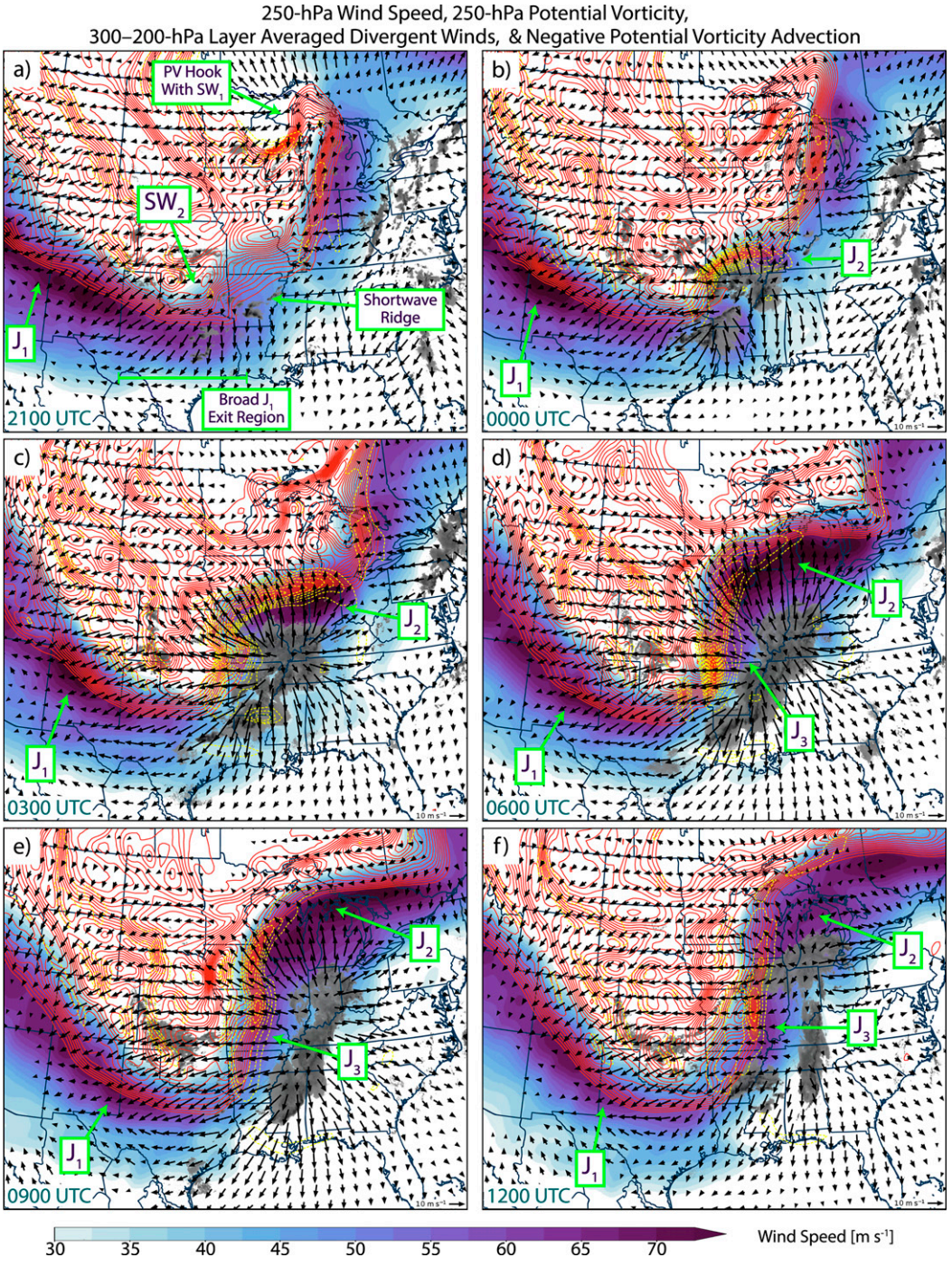

FIG. 3. Composite radar reflectivity > 20 dBZ (gray shading) overlaid with 250-hPa wind speed (purple shading; m s^{-1}), 250-hPa PV (orange contours; every 0.5 PVU ≥ 2 PVU), divergent winds averaged over the 300–200-hPa layer (vectors; m s^{-1}), and negative 250-hPa PV advection by the layer-averaged divergent winds (yellow dashed contours; contoured every 10^{-4} PVU s^{-1} ≤ -1×10^{-4} PVU s^{-1}) from the corresponding RUC 1-h forecast valid at (a) 2100 UTC 26 Apr, (b) 0000 UTC 27 Apr, (c) 0300 UTC 27 Apr, (d) 0600 UTC 27 Apr, (e) 0900 UTC 27 Apr, and (f) 1200 UTC 27 Apr 2011.

process that is sensitive to the MCS location relative to the baroclinic wave (e.g., Zhang and Harvey 1995; Stensrud 1996). Overall, numerous studies have demonstrated that latent heating may notably impact the structure and dynamics of baroclinic waves and extratropical cyclones (e.g., Kuo et al. 1991; Davis and Emanuel 1991; Whitaker and Davis 1994; Stoelinga 1996; Dickinson et al. 1997; Wernli et al. 2002).

b. Role of convection in upper-level flow modifications

Based on the environmental evolution presented in Part I, we hypothesize that complex scale interactions and upper-level flow modifications—including alterations to the height field and jetogenesis—occurred in response to the development of QLCS1 and QLCS2. Processes driving these modifications are now examined within the context of: 1) PV modifications by diabatic heating and upper-level convective outflow, and 2) flow imbalance and upper-level accelerations.

1) UPPER-LEVEL PV MODIFICATIONS AND JET STREAK FORMATION

Modifications to the upper-level PV field by convection occur through two primary processes: 1) the vertical redistribution of PV by latent heating (i.e., upper-level PV "erosion" owing to negative diabatic PV tendency), and 2) the vertical transport and subsequent horizontal advection of low-PV air by divergent upper-level outflow (hereinafter "negative PV advection"). Studies have demonstrated that latent heat release occurring near a background PV gradient and ahead of a midlatitude trough may promote downstream ridge amplification and a decrease in the wavelength of the large-scale pattern, which enhances forcing for ascent downstream from the trough while hindering its eastward propagation (e.g., Davis and Emanuel 1991; Stoelinga 1996; Stensrud 1996; Riemer et al. 2008; Steinfeld and Pfahl 2019; Winters et al. 2020). Furthermore, convection may steepen the PV gradient across the tropopause to promote upper-level jetogenesis (e.g., Archambault et al. 2013; Grams et al. 2013; Grams and Archambault 2016; Rowe and Hitchman 2016) and—in some instances—tropopause folding (e.g., Atallah and Bosart 2003; Rowe and Hitchman 2015).

The manner in which QLCS1 altered the PV distribution and upper-level flow pattern is explained with reference to Fig. 3. The onset of CI during the evening of 26 April was accompanied by the rapid development of strong convective outflow within broader J_1 exit region over the SGP and immediately downstream from SW_2 (Figs. 3a,b). Over eastern Texas, predryline convection produced convective outflow that largely opposed the background westerly flow within the upper-level jet (Figs. 3b,c). Additionally, widespread convection developed over Arkansas beneath a shortwave ridge and adjacent to a largely meridional upper-level PV gradient that was established in the wake of SW_1 (Fig. 3a; Part I). Following CI, diabatic PV erosion acting together with strong negative PV advection quickly sharpened the preexisting PV gradient over western Missouri and Arkansas (i.e., steepened the tropopause) and consequently induced J_2 immediately downstream (Figs. 3b–e). J_2 rapidly strengthened and advanced poleward with time in conjunction with sustained negative PV advection, which promoted upper-level ridge amplification and effectively shifted the longwave trough axis westward (by reducing its horizontal wavelength while counteracting its eastward progression; Figs. 2a–c). As QLCS1 grew upscale into a meridionally elongated system, the upper-level PV gradient to its west strengthened considerably, leading to the genesis of J_3 and ultimately the formation of a tropopause fold with SW_2 (hereinafter the "secondary tropopause fold"; Figs. 1c–f and 3c–f).

Just after 0900 UTC 27 April, QLCS2 formed ahead of SW_3 and adjacent to the tightened PV gradient that was established over Arkansas behind QLCS1 (Figs. 1e and 3e). Overall, QLCS2 produced upper-level flow modifications that were qualitatively similar but comparatively less substantial than those arising from QLCS1—likely due to its smaller spatial scale [O(500–600) km versus O(1200–1300) km for QLCS1] and the location where it formed relative to the background PV distribution, which had been dramatically altered by QLCS1. As depicted in Fig. 4a, QLCS2 had moved into northwestern Mississippi by 1300 UTC 27 April and was located east of SW_3 and immediately south of an eastward PV protrusion that corresponded to the amplifying SW_2. As a result of strong negative PV advection and diabatic PV erosion, a meso-α-scale ridge developed just downstream from SW_3, and the background PV gradient sharpened to the northwest of QLCS2 (Fig. 4b). Accordingly, J_4 formed over the Midwest in association with this sharpened PV gradient and advanced poleward with time, being situated ~800–1000 km downstream from the supercell outbreak that was commencing over the Southeast at 1900 UTC 27 April (Fig. 4c).

2) FLOW IMBALANCE AND UPPER-LEVEL ADJUSTMENTS

Within the context of flow imbalance and jet dynamics, we now further analyze these upper-level modifications. For a straight jet streak that obeys quasigeostrophic (QG) or semigeostrophic balanced dynamics (Hoskins 1975), a four-cell pattern of divergence and vertical motion develops in association with thermally direct and indirect transverse ageostrophic circulations that straddle the jet entrance and exit regions, respectively (e.g., Uccellini and Johnson 1979; Keyser and Shapiro 1986). Owing to complexities like flow curvature and thermal advection, the vertical motion distribution may deviate significantly from this simplified jet model while still maintaining thermal wind balance (e.g., Keyser and Shapiro 1986). However, jet streaks may instead be dynamically unbalanced and accompanied by considerable parcel accelerations, mass divergence, and vertical motions (e.g., Van Tuyl and Young 1982; Keyser and Johnson 1984; Uccellini et al. 1984; Rowe and Hitchman 2016). Unbalanced jets often are displaced downstream from their geostrophic counterparts, develop in response to abrupt changes in flow curvature, and induce an exceptionally strong LLJ via isallobaric forcing (e.g., Uccellini et al. 1984; Uccellini and Koch 1987; Koch and Dorian 1988).

A commonly used diagnostic for evaluating the degree to which mass and momentum fields are dynamically "balanced" is the nonlinear balance equation (NBE), which arises from a scale analysis of the divergence tendency equation and has proven applicability in highly curved flow and on relatively short time scales (e.g., Charney 1955; Raymond 1992; Zhang et al. 2000). The NBE residual diagnostic is given by

$$\mathrm{NBE} = 2J(u, v) + f\zeta - \beta u - \nabla^2\Phi, \tag{1}$$

where $J(u, v)$ is the Jacobian of the horizontal wind components, f is the Coriolis parameter, ζ is the relative vertical

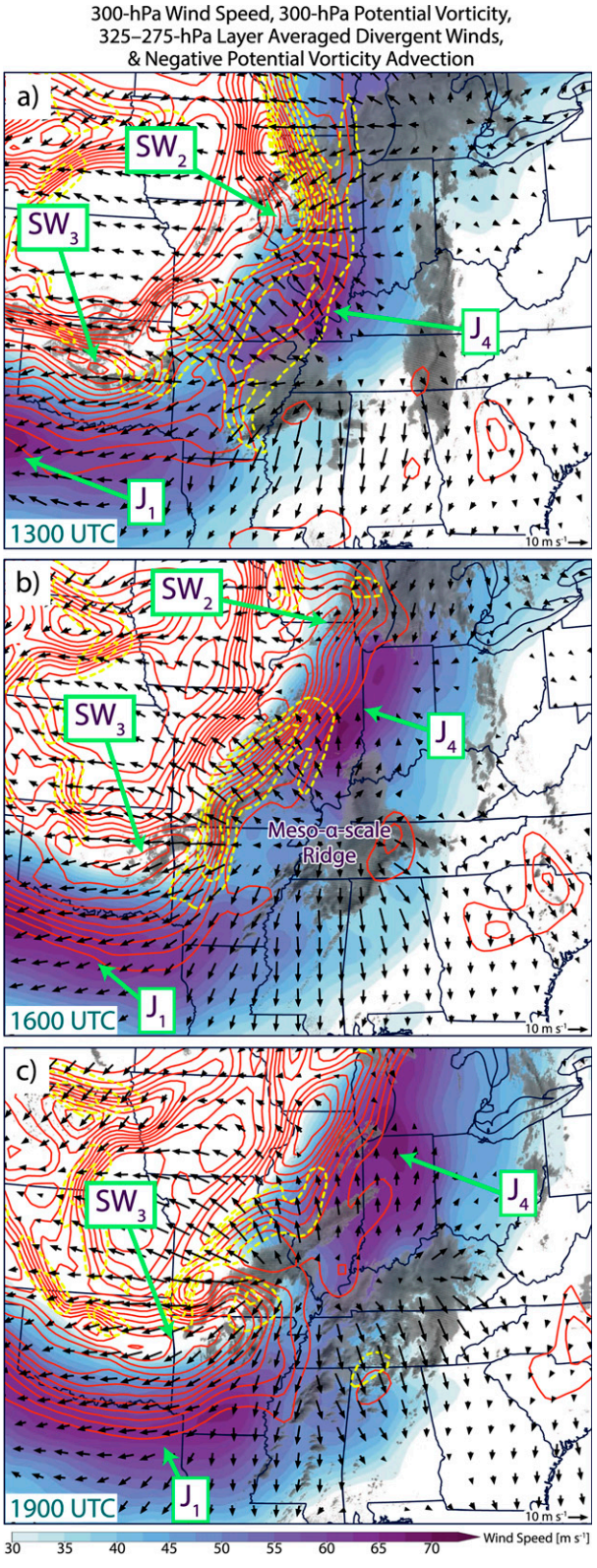

FIG. 4. Composite radar reflectivity > 20 dBZ (gray shading) overlaid with 300-hPa wind speed (purple shading; m s^{-1}), 300-hPa PV (orange contours; every 0.5 PVU ≥ 2 PVU), divergent winds averaged over the 325–275-hPa layer (vectors; m s^{-1}), and negative 300-hPa PV advection by the layer-averaged divergent winds (yellow dashed contours; contoured every 10^{-4} PVU s^{-1} ≤ -1×10^{-4} PVU s^{-1}) from the corresponding RUC 1-h forecast valid at (a) 1300, (b) 1600, and (c) 1900 UTC 27 Apr 2011.

vorticity, β is the Rossby parameter, and $\nabla^2\Phi$ is the 2D horizontal Laplacian of geopotential. Regions of large positive (negative) values of NBE residual are characterized by large divergence (convergence) tendency and thus do not satisfy nonlinear balance. The NBE and geostrophic wind fields presented herein were low-pass filtered using a Lanczos filter (Duchon 1979) with a cutoff wavelength (50% response) of 325 km to reduce the signal from gravity waves.

The development of strong upper-level ageostrophic motions and flow imbalance is described with reference to Figs. 5 and 6. The upper-level flow was largely balanced at 2000 UTC 26 April prior to the formation of QLCS1, when both an embedded upper-level wind maximum associated with SW_2—which was situated within the broader J_1 exit region—and its corresponding geostrophic wind maximum ("J_G") were collocated in the trough base over northern Texas (Figs. 5a and 6a). However, geopotential heights suddenly increased downstream from the trough base and within the jet exit region following CI, yielding a force imbalance that had three primary effects. First, parcel decelerations and mass convergence were dramatically enhanced west of the convection over eastern Texas (as inferred from the increased along-stream gradient in wind speed and large negative values of NBE residual), while the height gradient strengthened immediately upstream (Figs. 5b,c). Accordingly, the thermally indirect circulation about the jet exit region intensified as it became disrupted by convection. Second, the curvature of the height field was amplified, which—combined with the strengthened height gradient—induced notably strong (>100 kt; 1 kt ≈ 0.5 m s^{-1}) upstream-directed ageostrophic flow over the SGP. Finally, widespread convection over Arkansas—which formed south of the eastward trough extension that was established over the Midwest by SW_1—induced a strong isallobaric component that was preferentially directed northwestward *down the height gradient*, yielding considerable accelerations within the J_G exit region (Fig. 6b) and the rapid formation of J_2 downstream over the Midwest.

The onset of flow imbalance and strong upper-level accelerations was accompanied by a dramatic increase in mass divergence within the J_2 entrance region (as evidenced by the region of large positive NBE residual values in Figs. 5c,d), which reinforced the convection and facilitated its rapid upscale growth. Within 5 h of developing, the maximum 250-hPa wind speeds within J_2 had increased by more than 45 kt to a strength of 140 kt as QLCS1 and its outflow jet synchronously advanced poleward with time. Additionally, J_3 had formed within the strengthened height gradient to the west of QLCS1 by 0700 UTC 27 April, and strong cross-isohypse ageostrophic flow, implied accelerations, and upper-level divergence were prevalent over Arkansas at this time (Fig. 5d). Both of the jet streaks produced by QLCS1 were observed by a NOAA wind profiler located in Wolcott, IN, and

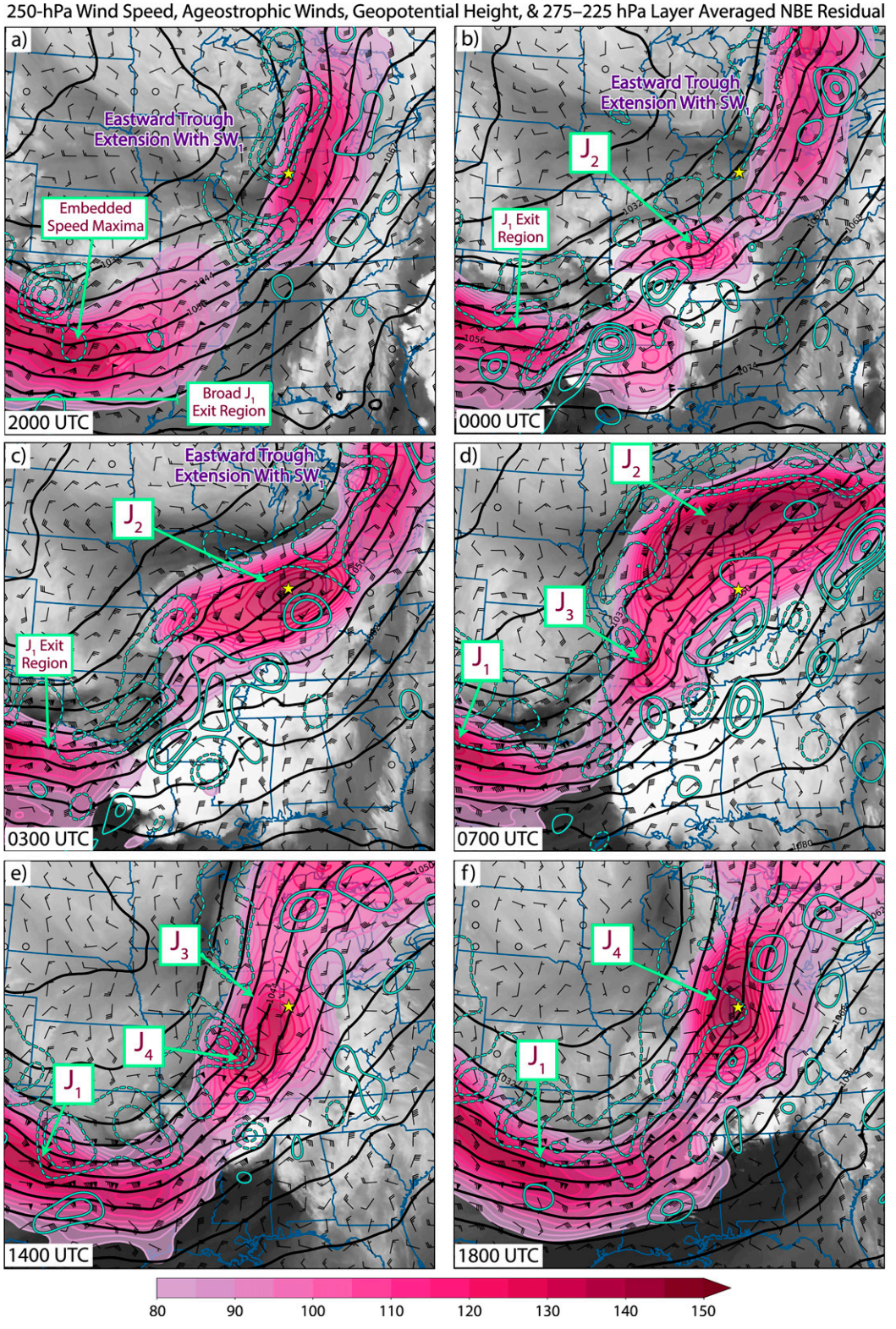

FIG. 5. *GOES-13* water vapor imagery overlaid with 250-hPa wind speed (shaded; kt), 250-hPa ageostrophic winds (barbs; kt), 250-hPa geopotential height (black contours; dam), and 275–225-hPa layer-averaged NBE residual (positive values shown by solid cyan contours every 1×10^{-8} s$^{-2} \geq 2 \times 10^{-8}$ s^{-2}; negative values shown by dashed cyan contours every 1×10^{-8} s$^{-2} \leq -2 \times 10^{-8}$ s^{-2}) from the corresponding RUC 1-h forecasts valid at (a) 2000 UTC 26 Apr, (b) 0000 UTC 27 Apr, (c) 0300 UTC 27 Apr, (d) 0700 UTC 27 Apr, (e) 1400 UTC 27 Apr, and (f) 1800 UTC 27 Apr 2011. The NBE field was low-pass filtered. The Wolcott, IN, wind profiler location is denoted by the yellow marker.

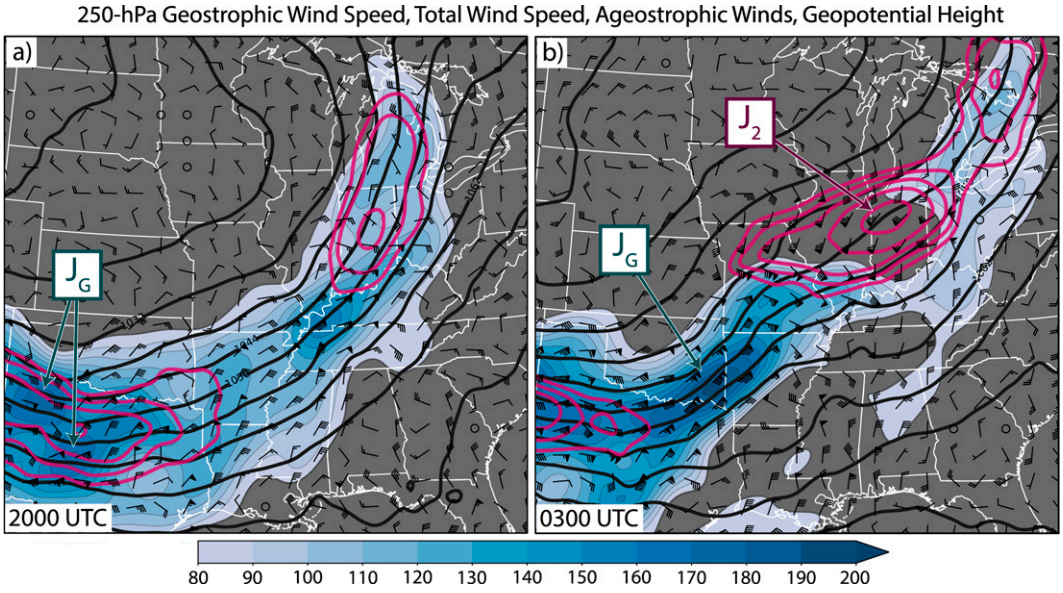

FIG. 6. The 250-hPa geostrophic wind speed (shaded; kt), 250-hPa total horizontal wind speed (magenta contours; every 10 kt ≥ 100 kt), 250-hPa ageostrophic winds (barbs; kt), and 250-hPa geopotential height (black contours; dam) from the corresponding RUC 1-h forecasts valid at (a) 2000 UTC 26 Apr and (b) 0300 UTC 27 Apr 2011. Geostrophic wind maxima are denoted by the teal arrows. The geostrophic wind fields were low-pass filtered.

are evident in the time–height diagram of wind speed shown in Fig. 7.

In a similar manner, J_4 developed and quickly intensified over the Midwest in response to strong cross-isohypse convective outflow and implied accelerations that resulted from QLCS2 (Figs. 5e,f). As QLCS2 grew upscale throughout the morning, the system remained coupled to the right-entrance region of J_4, which was characterized by strong upper-level divergence and flow imbalance as the jet streak was continually bolstered by convective outflow. J_4 had strengthened to more than 140 kt by 1800 UTC 27 April (Fig. 5f) and was also observed by the wind profiler in Wolcott (Fig. 7).

c. *Mid- to upper-tropospheric modifications and tropopause folding*

Recall that J_3 formed in association with tropopause steepening behind QLCS1 following its upscale growth. We now describe how this evolution related to the development of the secondary tropopause fold and associated amplification of SW_2 over the Midwest. Shown in Fig. 8 are the potential temperature and geostrophic potential temperature advection fields averaged over the 550–450-hPa layer between 0700 and 1900 UTC 27 April. As QLCS1 grew progressively upscale overnight, the potential temperature gradient $\nabla\theta$ within the upper and middle troposphere strengthened along the system's northern and western flanks owing to differential thermal advection and diabatic heating. This resultant frontogenesis would induce a thermally direct transverse ageostrophic circulation about the baroclinic zone such that subsidence was enhanced on the polar (cool) side to yield downward transport of high-PV air and tropopause steepening (e.g., Keyser and Shapiro 1986). Consistent with this expected evolution, a distinct corridor of enhanced midlevel $\nabla\theta$ had developed below the steepened tropopause accompanying J_3 by 0700 UTC 27 April (Figs. 3d and 8a) and was paralleled by a band of midlevel subsidence (not shown), with maximum downward motion collocated with a 400-hPa PV anomaly over Missouri that represented the developing tropopause fold (Fig. 9a).

Geostrophic cold advection (CAA) increased behind QLCS1 and within the strengthening front as the system moved northeastward throughout the morning (Figs. 8a–c). This supported QG forcing for subsidence and upper-level height falls, and a distinct region of 400-hPa height falls remained situated above the strongest midlevel geostrophic CAA over the Midwest during this period (Figs. 9a–c). Furthermore, Keyser and Shapiro (1986) described how geostrophic CAA occurring along an upper-level front shifts the secondary ageostrophic circulation such that subsidence forms beneath the jet axis and tilting effects become frontogenetical—a positive feedback that produces stronger subsidence and tropopause folding. Accordingly, the region of geostrophic CAA became increasingly collocated with the strongest midlevel subsidence behind QLCS1 over time (not shown), and $\nabla\theta$ further intensified in consequence—yielding greater geostrophic CAA, continued amplification of SW_2 (via sustained forcing for upper-level height falls), and further deepening of the secondary tropopause fold beneath J_3 (Figs. 8 and 9). Overall, the longevity of differential vertical motions that coincided with the western periphery of QLCS1 and a tightened upper-level PV gradient played a critical role in this evolution. Ultimately, the amplification of SW_2 supported greater forcing for ascent over the QLCS1 stratiform region and surface cyclogenesis with L_2, which we discuss in section 4d. This progression was supported by the wind

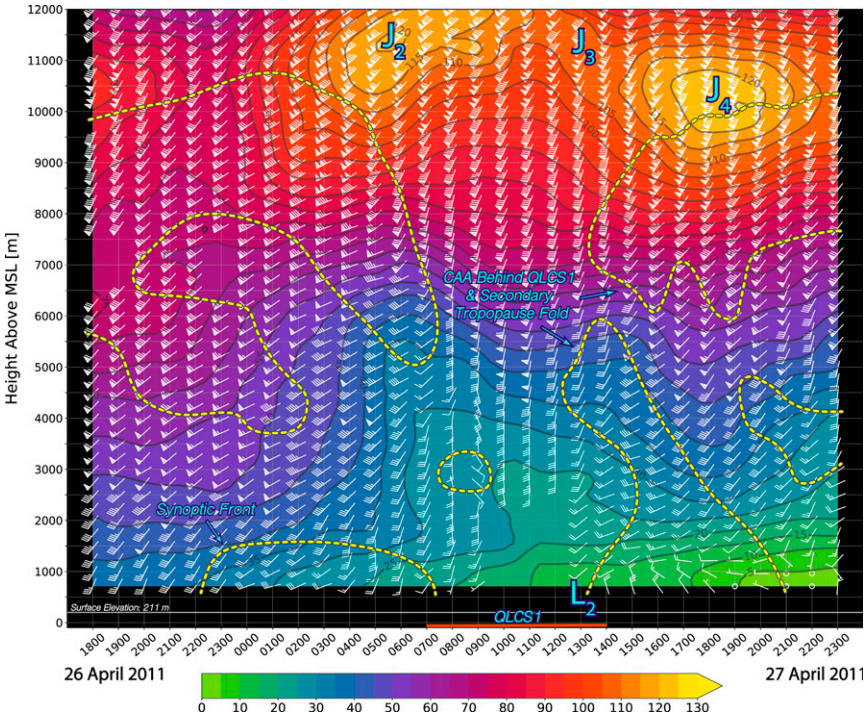

FIG. 7. Time–height diagram of objectively analyzed horizontal wind speed (shaded; kt) and observed horizontal winds (barbs; kt) from the NOAA wind profiler located in Wolcott. Regions of derived geostrophic cold advection are denoted by the yellow dashed contours. The procedure used to produce this diagram is described in Part I. The wind profiler location is shown in Fig. 6.

profiler observations from Wolcott, which depicted a deep region of derived geostrophic CAA behind QLCS1 and below J_3 and the subsequent passage of L_2 at ~1300 UTC 27 April (Fig. 7).

As a result of the amplification of SW_2, the large-scale flow curvature and overall diffluence were diminished downstream from the longwave trough and SW_3, yielding broad and fairly unidirectional southwesterly flow over the Southeast in the wake of QLCS1 (Figs. 9b–d). The mid- to upper-tropospheric flow was further altered following the formation and upscale growth of QLCS2, which induced a meso-α-scale region of height rises and midlevel warming (Figs. 8c,d and 9c,d) immediately downstream from SW_3 and within the J_1 exit region during the morning and early afternoon (Fig. 10). Accordingly, QLCS2 effectively amplified the cyclonic perturbations accompanying SW_2 and SW_3 and enhanced the *mesoscale* flow curvature ahead of SW_3 prior to the supercell outbreak.

The midlevel warming accompanying QLCS2 intensified and reoriented the background thermal gradient to its north and west, promoting increased geostrophic CAA (and thus forcing for height falls) ahead of SW_3 (Figs. 8c,d and 9c,d). Furthermore, the 400-hPa height rises stemming from QLCS2 strengthened (weakened) the height gradient on the cyclonic (anticyclonic) flank of the jet (Figs. 9c,d) while forking the J_1 exit region into two branches around the system (Fig. 10). The northern branch—which was supported by the bolstered height gradient—was characterized by a narrow corridor of ~90–105 kt south-southwesterly winds and large positive values of NBE residual at 1500 UTC 27 April. Accordingly, accelerations were occurring within this branch as it pivoted cyclonically over time, yielding an extensive region of strengthened winds by 1800 UTC 27 April. Conversely, the southern branch was diverted over the Southeast and comprised weaker (~80–95 kt at 1800 UTC 27 April) and considerably more veered southwesterly winds. Large negative values of NBE residual, strong equatorward-directed ageostrophic flow, and implied decelerations accompanied this southern branch and—combined with the thermally indirect ageostrophic circulation attending the upper-level J_1 exit region (Figs. 5e,f)—supported midlevel subsidence over much of the Southeast prior to the afternoon supercell outbreak.

d. Low-level jet evolution and surface cyclogenesis

Recall that the low-level flow intensification that commenced immediately after QLCS1 formed was postulated to have supported this system's exceptional severity. Prior to any upper-level flow modifications by QLCS1, a broad region of southerly 30–40-kt winds extended from central Texas into Alabama at 850 hPa (Fig. 11a). However, the sudden increase in upper-level divergence (and resultant low-level height falls) that

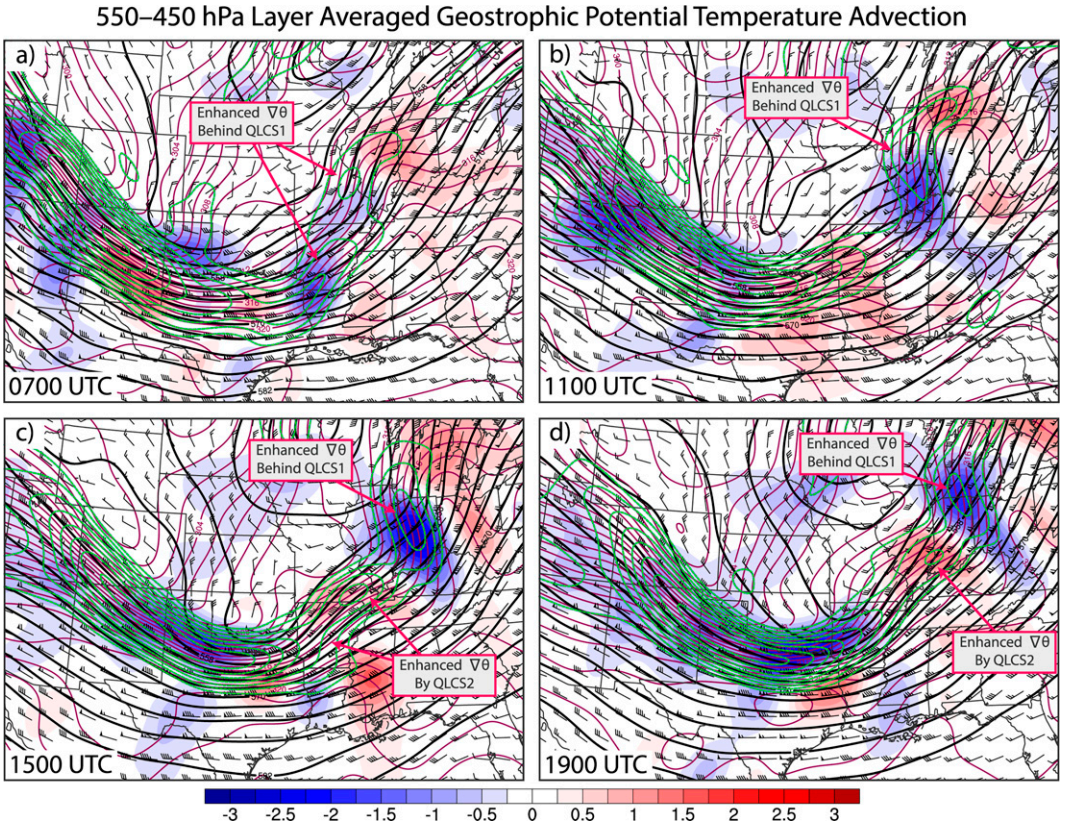

FIG. 8. Geostrophic potential temperature advection averaged over the 550–450-hPa layer (shaded; K h^{-1}), 550–450-hPa layer-averaged potential temperature (magenta contours; K), 550–450-hPa layer-averaged geostrophic winds (barbs; kt), 500-hPa geopotential height (black contours; dam), and 550–450-hPa layer-averaged potential temperature gradient [dashed green contours; every 0.5 K $(100\ km)^{-1} \geq 1.5$ K $(100\ km)^{-1}$] from the corresponding RUC 1-h forecasts valid at (a) 0700, (b) 1100, (c) 1500, and (d) 1900 UTC 27 Apr 2011. The plotted fields were low-pass filtered with a cutoff horizontal wavelength of 500 km.

accompanied the formation of J_2 caused the LLJ to rapidly strengthen and expand northward with time ahead of QLCS1 (Figs. 5b,c and 11b,c). Specifically, the LLJ was tightly coupled to the highly unbalanced J_2 entrance region, and its intensification and poleward advancement occurred as an isallobaric response to the intensification and poleward advancement of J_2. By 0700 UTC 27 April, an elongated corridor of 60–75-kt 850-hPa winds extended into the Ohio Valley, which was situated beneath the J_2 entrance region and accompanying maximum in NBE residual (Figs. 5d and 11d) and coincided with low-level height falls of more than 20 m $(4\ h)^{-1}$ (Fig. 12a).

Additionally, cyclogenesis corresponding to L_2 commenced over the Midwest below the J_2 entrance region and ahead of SW_2 as an upshear tilt in the PV field associated with the secondary tropopause fold developed behind QLCS1 (Fig. 13). At 0900 UTC 27 April, the 2-PVU (1 PVU = 10^{-6} K kg^{-1} m^2 s^{-1}) contour within the tropopause fold extended down to 500 hPa and was ~200 km west of vertically aligned midlevel and low-level PV anomalies corresponding to a diabatically generated MCV and a quasi-stationary front, respectively (Figs. 13a,c). By 1200 UTC 27 April, a coherent ~995-hPa surface low had formed along the surface front and remained collocated with the overlying diabatic PV anomaly and downshear from the tropopause fold (Figs. 13d,f). This low L_2 deepened over time in response to sustained low-level height falls (Figs. 12b–d) ahead of SW_2 and beneath the highly divergent J_2 entrance region (Figs. 5e,f and 9b–d). Meanwhile, L_3 was slowly reorganizing ahead of SW_3 throughout this period, yielding two subsynoptic-scale lows that were separated by approximately 1000 km at 1500 UTC 27 April (Fig. 12c). Low event L_3 was not supported by appreciable height falls until SW_3 began to noticeably amplify over Arkansas (i.e., near the beginning of the supercell outbreak), after which time L_3 gradually deepened and became increasingly compact (Fig. 12d).

In the hours before the supercell outbreak, the LLJ structure reflected the presence of both lows and was influenced by convectively driven flow modifications aloft in addition to the approaching SW_3. At 1400 UTC 27 April, an uninterrupted corridor of 850-hPa winds greater than 50 kt extended from the Gulf Coast into the Great Lakes region and included two embedded LLJ maxima—the southernmost of which comprised 65–80-kt winds over the Southeast (Fig. 11e). In Part I, we attributed this secondary maximum to rapid low-level accelerations that occurred following the formation of QLCS2 ahead of SW_3.

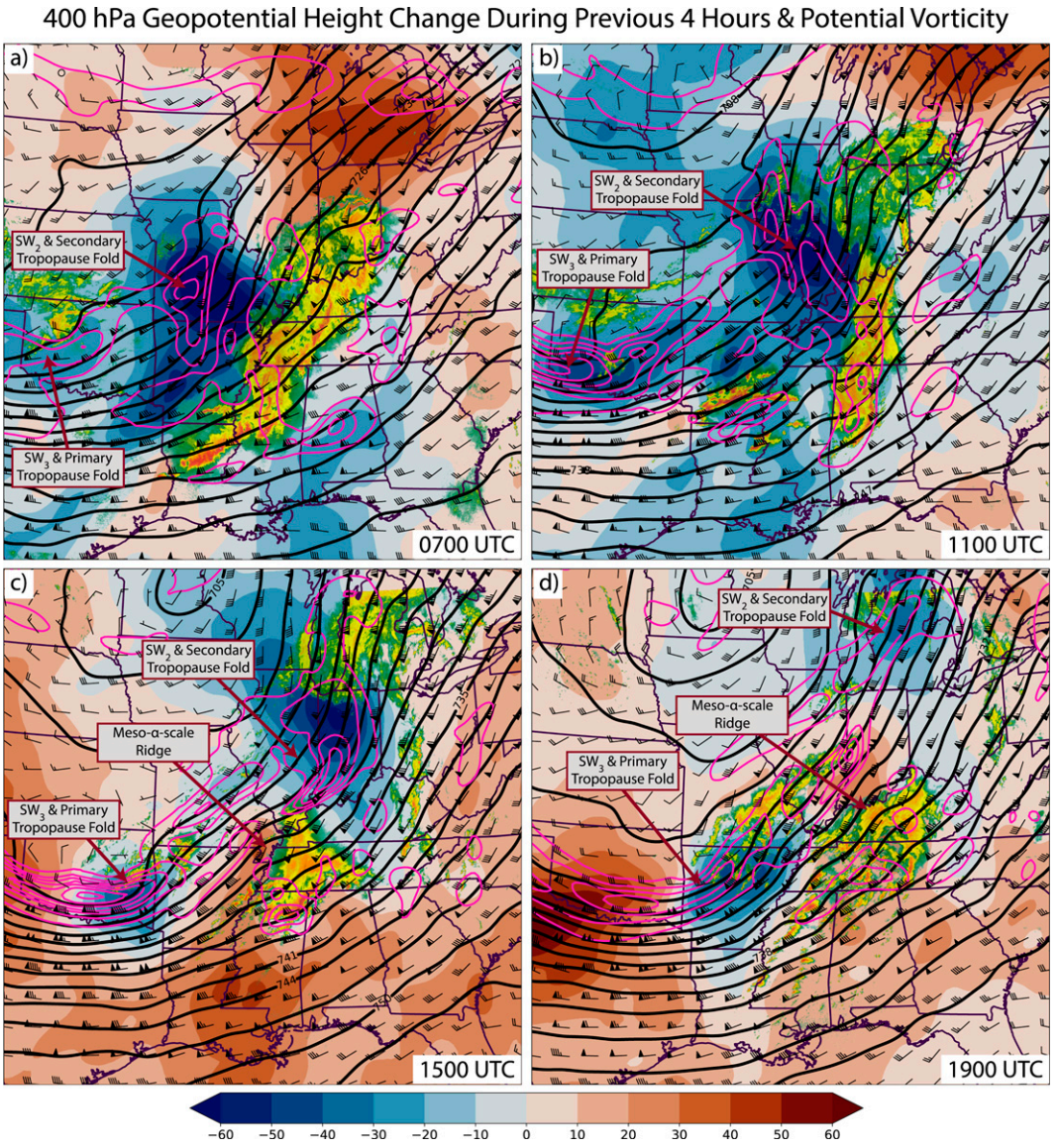

FIG. 9. Composite radar reflectivity > 20 dB*Z* overlaid with 400-hPa geopotential height change during the previous 4 h (shaded; m), 400-hPa potential vorticity (pink contours; every 1 PVU ≥ 1 PVU), 400-hPa geopotential height (black contours; dam), and 400-hPa horizontal winds (barbs; kt) from the corresponding RUC 1-h forecasts valid at (a) 0700, (b) 1100, (c) 1500, and (d) 1900 UTC 27 Apr 2011.

Indeed, the LLJ further strengthened throughout the morning as a coherent region of 900-hPa height falls of more than 20 m (4 h)$^{-1}$ developed within the QLCS2 inflow environment and expanded poleward with time (Figs. 12b–d). By the beginning of the supercell outbreak, a mesoscale corridor comprising 850-hPa winds of 70–80 kt and considerable cross-isohypse ageostrophic flow was centered over middle Tennessee and northwestern Alabama (Fig. 11f) beneath an area of large positive NBE residual and pronounced upper-level divergence accompanying the right-entrance region of J_4 and the split J_1 exit region (Figs. 5f and 10c). We note that the greatest low-level wind speeds throughout this evolution were displaced to the north and northwest of the strongest height gradient—indicative of the highly ageostrophic and unbalanced nature of the LLJ over the Southeast. This notably strong and highly ageostrophic LLJ present at the onset of the supercell outbreak was therefore partially attributable to isallobaric forcing that accompanied the formation of QLCS2, which augmented the background forcing ahead of SW_3 and supplemented the persistent low-level flow enhancement that stemmed from QLCS1.

e. Relationship of flow modifications to vertical shear profiles during the supercell outbreak

We now evaluate how these flow modifications influenced the vertical shear profiles over the Southeast during the

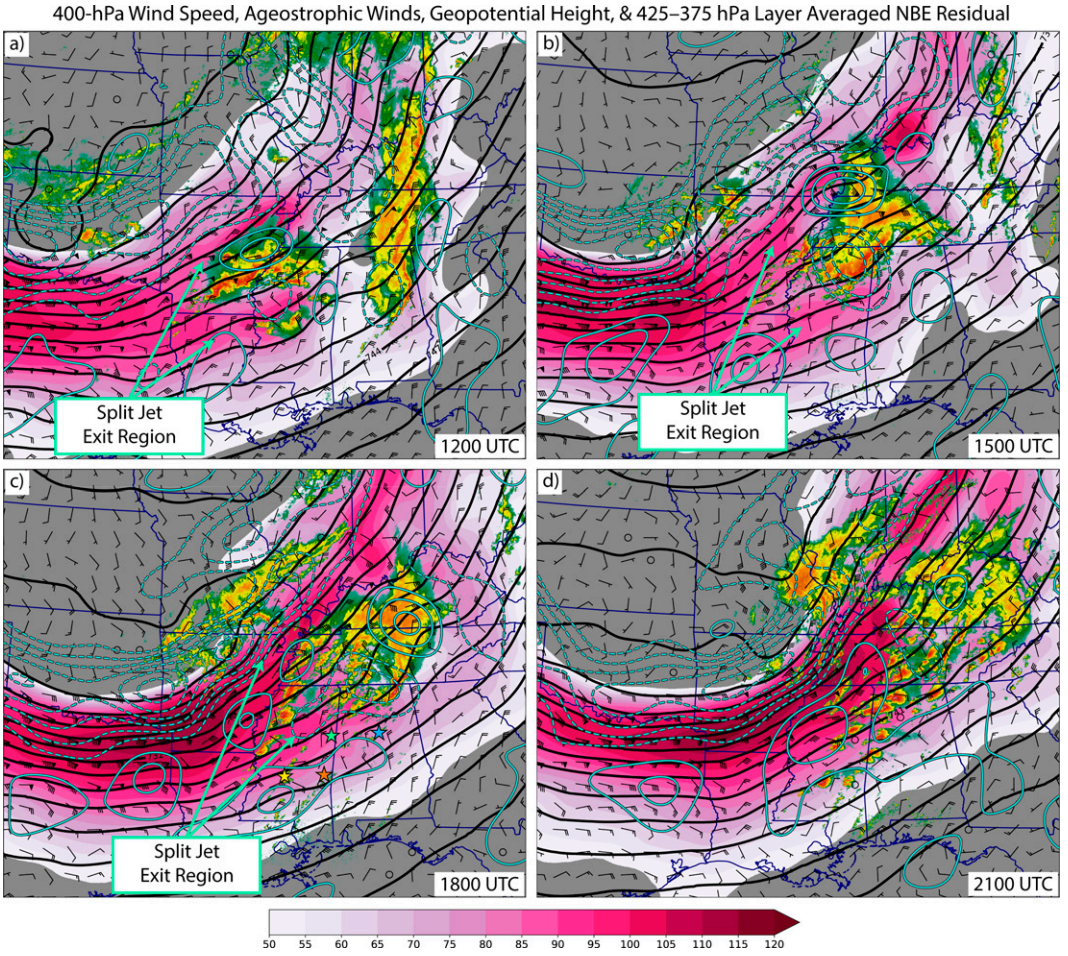

FIG. 10. Composite radar reflectivity > 20 dBZ overlaid with 400-hPa horizontal wind speed (shaded; kt), 400-hPa geopotential height (black contours; dam), 400-hPa ageostrophic winds (barbs; kt), and 425–375-hPa layer-averaged NBE residual (positive values shown by solid cyan contours every 1×10^{-8} s$^{-2} \geq 1 \times 10^{-8}$ s^{-2}; negative values shown by dashed cyan contours every 1×10^{-8} s$^{-2} \leq -1 \times 10^{-8}$ s^{-2}) from the corresponding RUC 1-h forecasts valid at (a) 1200, (b) 1500, (c) 1800, and (d) 2100 UTC 27 Apr 2011. The locations of Columbus, MS; Birmingham, AL; Jackson, MS; and Meridian, MS, are shown in (c) with the green, blue, yellow, and orange markers, respectively.

afternoon supercell outbreak. Numerous studies have collectively established that long-lived, right-moving supercells (in the NH) are favored within environments that contain strong deep-layer vertical wind shear and a shear vector that veers with height (particularly throughout the lower troposphere), yielding a "long" hodograph with appreciable clockwise curvature and SRH (e.g., Rotunno and Klemp 1982; Weisman and Klemp 1984; Davies-Jones 1984; Rotunno and Klemp 1985; Brooks and Wilhelmson 1993; Weisman and Rotunno 2000; McCaul and Weisman 2001). Furthermore, shear and SRH computed over shallow near-surface layers (i.e., 0–500 m and 0–1 km) have proven to discriminate well between tornadic and nontornadic supercell environments (e.g., Rasmussen 2003; Thompson et al. 2003; Markowski et al. 2003; Coffer et al. 2019).

Although these studies defined what constitutes a favorable shear environment for supercells and tornadoes, less attention has been given to explicitly diagnosing the processes responsible for creating such hodographs within tornado outbreak environments[2] (e.g., Roebber et al. 2002; Gold and Nielsen-Gammon 2008). In the conceptually straightforward scenario of geostrophic flow and thermal wind balance, the vertical wind shear is solely a function of the background thermal gradient. Accordingly, the magnitude of the geostrophic shear depends upon the strength of the background baroclinity, and the geostrophic hodograph shape is determined by how the orientation and strength of the thermal gradient vary with height. Through this relationship, meteorologists frequently assume that much of the hodograph curvature found in tornado environments is due to geostrophic veering in the presence of ample warm advection (WAA; e.g., Maddox et al. 1980; Maddox

[2] We are specifically concerned with external processes that preceded CI within a particular tornadic episode.

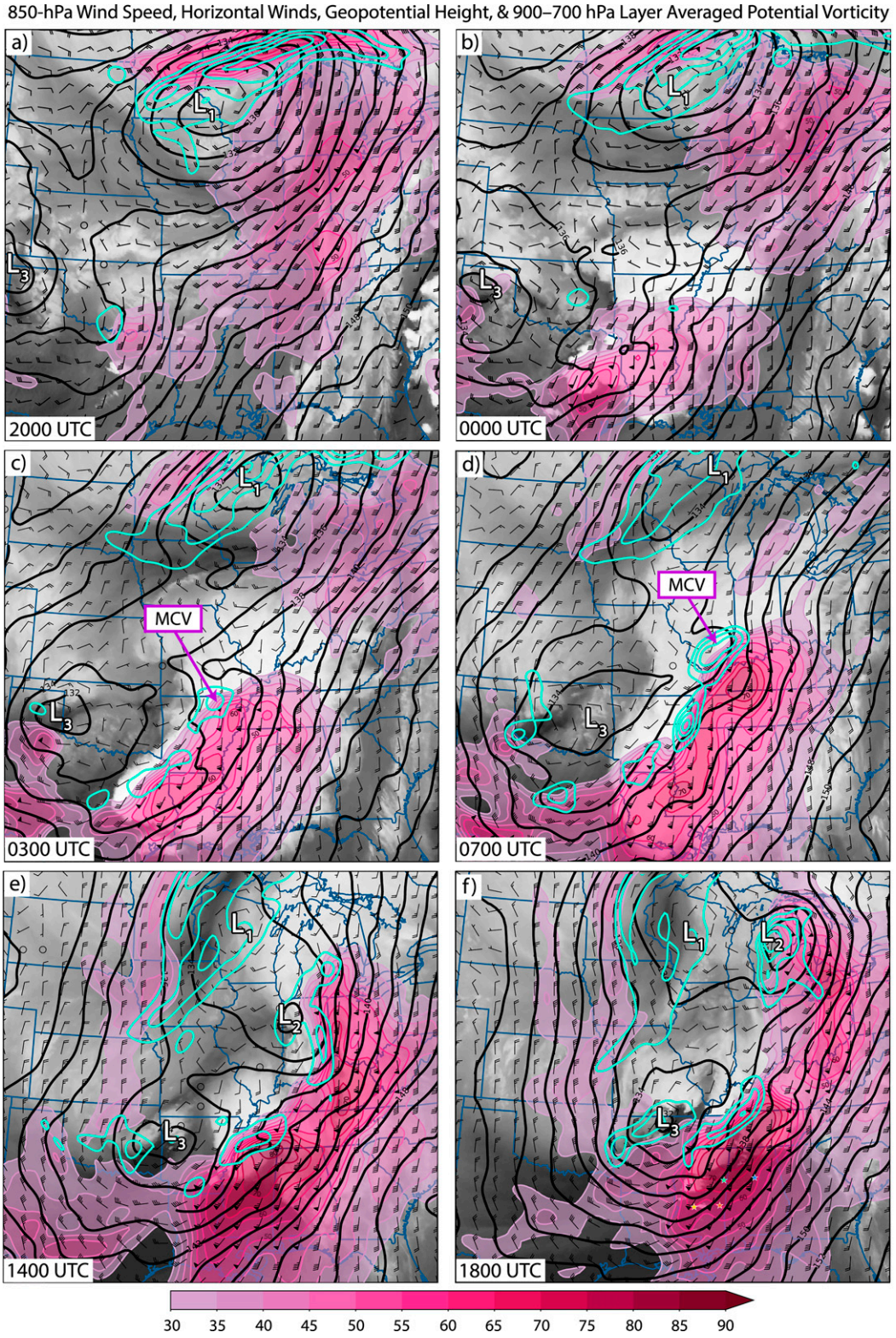

FIG. 11. *GOES-13* water vapor imagery overlaid with 850-hPa wind speed (shaded; kt), 850-hPa horizontal winds (barbs; kt), 850-hPa geopotential height (contours; dam), and 900–700-hPa layer-averaged PV (cyan contours; every 0.5 PVU ≥ 1 PVU) from the corresponding RUC 1-h forecasts valid at (a) 2000 UTC 26 Apr, (b) 0000 UTC 27 Apr, (c) 0300 UTC 27 Apr, (d) 0700 UTC 27 Apr, (e) 1400 UTC 27 Apr, and (f) 1800 UTC 27 Apr 2011. The locations of Columbus, Birmingham, Jackson, and Meridian are shown in (f) using the same notation as in Fig. 10.

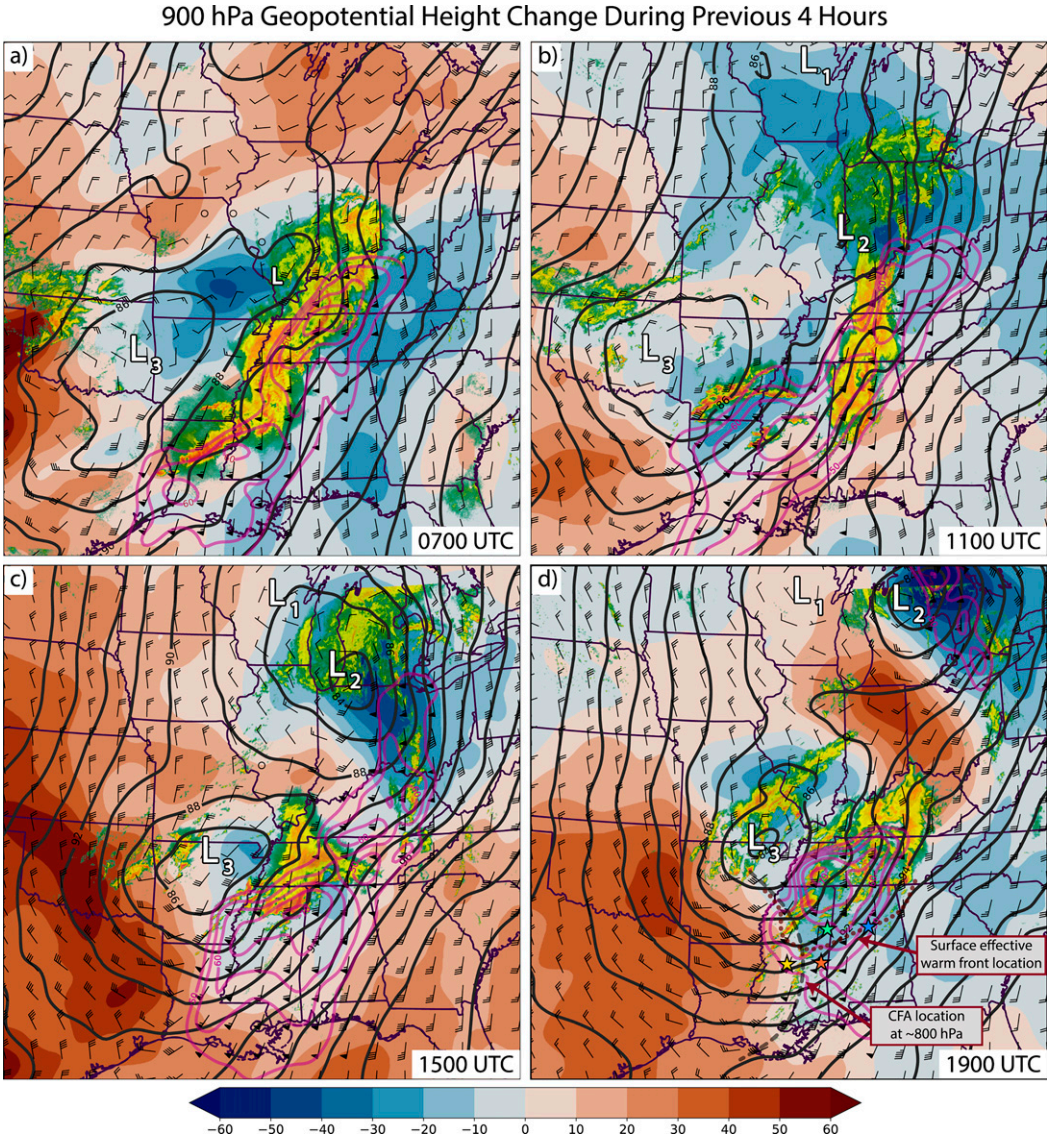

FIG. 12. Composite radar reflectivity > 20 dBZ overlaid with 900-hPa geopotential height change during the previous 4 h (shaded; m), 900-hPa geopotential height (black contours; dam), 900-hPa wind speed (magenta contours; every 5 kt ≥ 50 kt), and 900-hPa horizontal winds (barbs; kt) from the corresponding RUC 1-h forecasts valid at (a) 0700, (b) 1100, (c) 1500, and (d) 1900 UTC 27 Apr 2011. The locations of Columbus, Birmingham, Jackson, and Meridian are shown in (d) using the same notation as in Fig. 10. The manually analyzed positions of the effective warm front and CFA are shown with the red dotted line and gray dashed line, respectively, based upon Fig. 14 in Part I.

and Doswell 1982; Doswell and Bosart 2001; Markowski and Richardson 2011). However, tornado outbreaks—including the one described herein—often occur in the warm sector where baroclinity is generally weak (e.g., Hoxit and Chappell 1975; Koch et al. 1998; Thompson and Edwards 2000; Bunkers et al. 2006; Garner 2012). Furthermore, severe weather environments typically comprise jet streaks and may evolve rapidly (i.e., the flow is dynamically unbalanced), yielding large pressure tendencies and strong accelerations (e.g., Kocin et al. 1986; Zack and Kaplan 1987; Kaplan et al. 1998). In such environments, the ageostrophic component may contribute significantly to the vertical shear profile such that the oft-assumed thermal wind relationship has limited applicability (e.g., Doswell 1991; Doswell and Bosart 2001). The effects of flow curvature and friction also promote ageostrophic motions—the latter of which tends to induce or enhance veering throughout the PBL and increase low-level hodograph curvature (e.g., Maddox et al. 1980; Davies-Jones 1984; Banacos and Bluestein 2004; Markowski and Richardson 2011).

In Part I, we noted that the vertical shear, hodograph shapes, and SRH values during the afternoon were more than

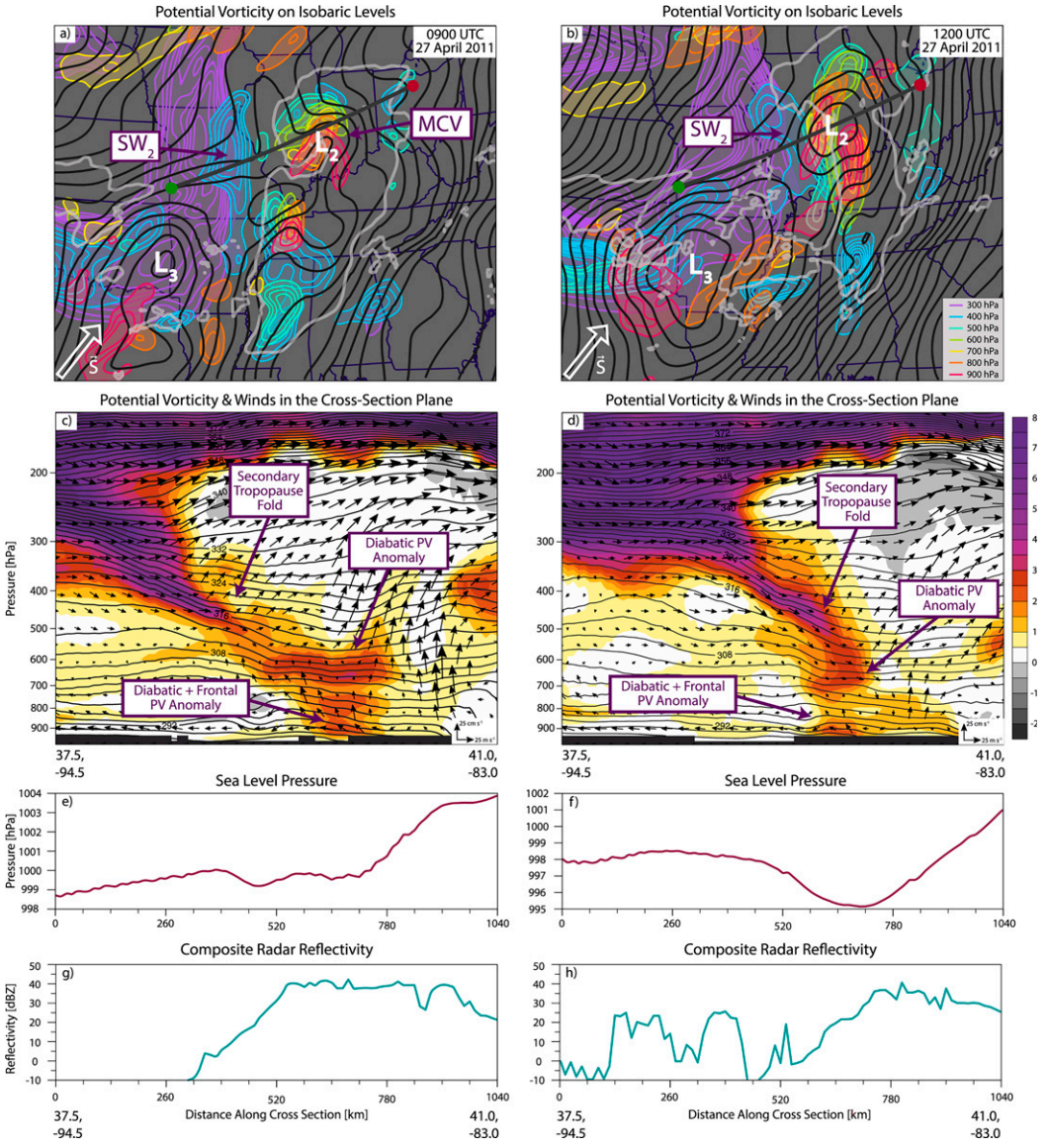

FIG. 13. RUC depiction of PV calculated on different isobaric levels (colored contours; every 0.5 PVU ≥ 1.5 PVU), SLP (black contours; hPa), and simulated composite radar reflectivity (white contours; 25 dBZ) at (a) 0900 and (b) 1200 UTC; vertical cross sections of PV (shaded; PVU), potential temperature (gray contours; K), and total winds within the plane of the cross section (vectors; scale shown on the plots) at (c) 0900 and (d) 1200 UTC; SLP along the cross-sectional path at (e) 0900 and (f) 1200 UTC; simulated composite radar reflectivity along the cross-sectional path at (g) 0900 and (h) 1200 UTC. The cross-sectional path is denoted by the dark-gray line in (a) and (b) and is oriented from the green (left) to red (right) filled circles at each end. The estimated mean shear vector over the 1000–400-hPa layer within the vicinity of L_2 is depicted by the arrow. Note that the *y*-axis ranges differ between (e) and (f).

sufficient for persistent mesocyclones and tornadoes and were largely attributed to the deflection of the midlevel jet over the Southeast by QLCS2 and the accumulated low-level flow intensification that accompanied the formation of QLCS1 and QLCS2. Knupp et al. (2014) also emphasized these notable shear profiles and related their existence—specifically over northern Alabama at 2100 UTC 27 April—to isallobaric forcing ahead of SW_3, friction, and the thermally direct circulation accompanying the effective warm front. However, we stress that strong low-level shear and high SRH were established over the Southeast several hours prior to 2100 UTC 27 April (see Fig. 12 of Part I), when SW_3 remained far upstream. To assess the relative importance of ageostrophic motions—due to both convective feedbacks and other processes—on the shear profiles *at the beginning of the supercell outbreak*, we show in Fig. 14 hodographs of the total horizontal wind, geostrophic wind component, and ageostrophic wind component at 1900 UTC 27 April from four locations: Columbus, Mississippi;

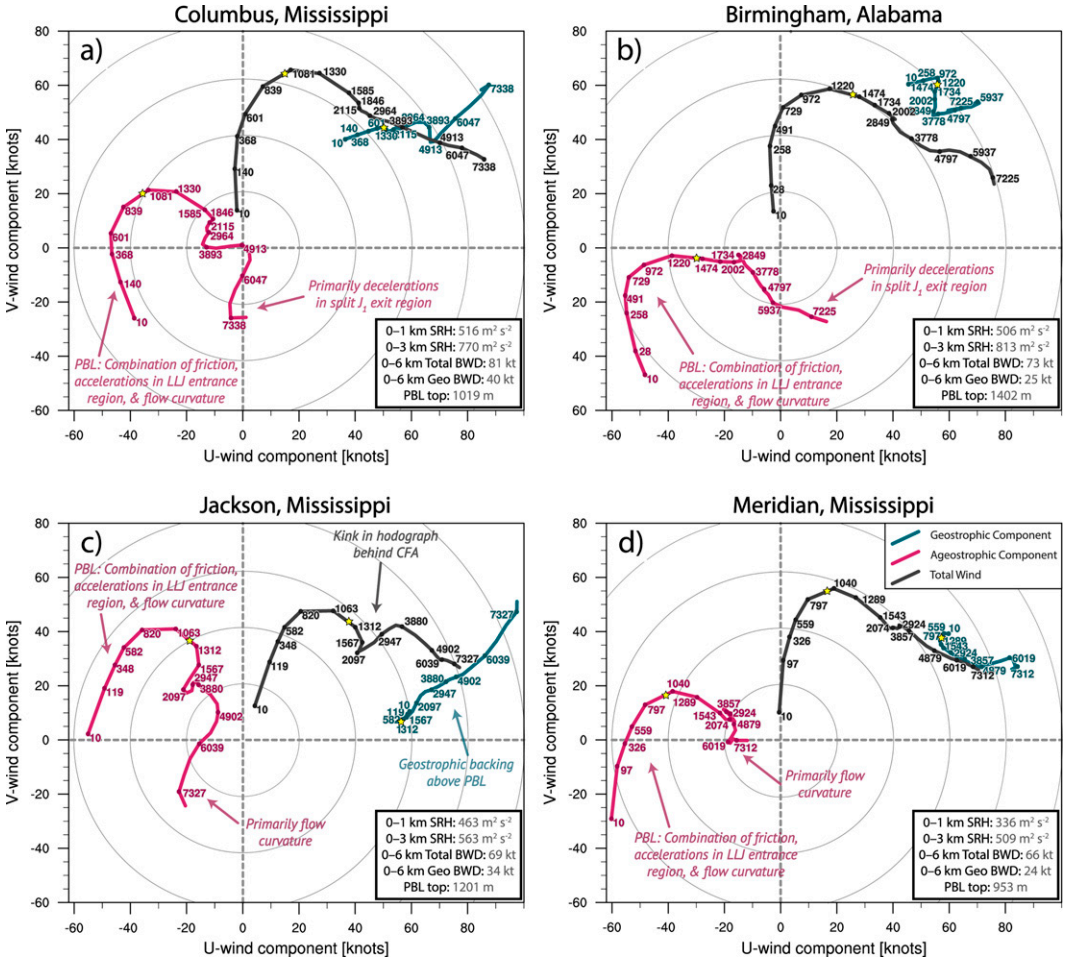

FIG. 14. Hodographs showing the vertical profiles of the total horizontal wind (gray; kt), geostrophic wind component (blue; kt), and ageostrophic wind component (magenta; kt) at (a) Columbus, (b) Birmingham, (c) Jackson, and (d) Meridian from the RUC 1-h forecast valid at 1900 UTC 27 Apr 2011. The hodograph labels represent height AGL (m). The yellow star denotes the approximate height of the PBL. Wind and geopotential height fields were low-pass filtered with a cutoff horizontal wavelength of 325 km prior to computing the geostrophic and ageostrophic components. The hodograph locations are displayed in Fig. 11f.

Jackson, Mississippi; Meridian, Mississippi; and Birmingham, Alabama.

Overall, the geostrophic hodographs from all four locations exhibited strong southwesterly flow (particularly within the middle-to-upper troposphere), which developed following the downstream amplification of SW_2 and was furthered by the flow modifications produced ahead of SW_3 by QLCS2. Geostrophic veering (and implied WAA) was apparent in the hodographs from Columbus, Birmingham, and Meridian, but the accompanying geostrophic shear was largely unidirectional and generally weak at all levels—consistent with the expectation of minimal baroclinity and thermal advection in the warm sector—and alone would not likely support a prolific tornado outbreak (e.g., Rasmussen and Blanchard 1998; Rasmussen 2003; Thompson et al. 2003). Conversely, the geostrophic hodograph from Jackson—which was located behind the CFA but within the surface warm sector (Fig. 12d)—exhibited backing with height (and implied CAA) beginning near the top of the PBL and extending throughout the depth of the troposphere. Notably, only subtle backing within a shallow layer was evident in the total wind hodograph and existed exclusively due to a "kink" in the ageostrophic hodograph at approximately 1.5–3 km, which corresponded to the elevated layer of CAA analyzed behind the CFA in Fig. 13 of Part I.

At all locations, the shape of the hodograph and the strength of the vertical wind shear—particularly throughout the lower to middle troposphere—were dictated almost entirely by the ageostrophic wind profile. The ageostrophic hodographs over the lowest ~1.5–2 km exhibited considerable low-level shear and clockwise curvature as the ageostrophic wind veered with height. The near-surface ageostrophic winds were incredibly strong (i.e., up to 67 kt at 10 m; Fig. 14d), largely opposed their

TABLE 1. WRF-ARW Model, version 4.2.1, configuration and physics parameterizations.

Configuration	Outer domain	Inner domain
Duration	1800 UTC 26 Apr–0600 UTC 28 Apr 2011	1800 UTC 26 Apr–0600 UTC 28 Apr 2011
Horizontal grid spacing	15 km	3 km
No. of grid points	420 × 320	1151 × 981
No. of vertical levels	70	70
Model top	10 hPa	10 hPa
ICs/BCs	GFS/GFS	GFS/Outer domain
Cumulus	New Tiedtke (LH only)	None
PBL	MYNN	MYNN
LSM	Unified Noah	Unified Noah
Microphysics	Thompson	Thompson
Shortwave radiation	RRTMG	RRTMG
Longwave radiation	RRTMG	RRTMG

geostrophic counterparts, and resulted predominantly due to a combination of friction (the effects of which diminished with height throughout the PBL) and flow curvature. However, a large cross-isohypse component of the ageostrophic flow (i.e., the component orthogonal to the geostrophic wind) also existed throughout the lower troposphere (including above the PBL) and was related primarily to accelerations occurring within the LLJ entrance region (Figs. 11f and 12d). Aloft, ageostrophic component winds greater than 25 kt were found above 7 km in Columbus and Birmingham (owing primarily to decelerations within the southern split branch of J_1) and in Jackson (owing primarily to flow curvature), which further improved the shape of the total wind hodograph.

Overall, strong ageostrophic motions that veered with height throughout the lower troposphere combined with appreciable deep-layer southwesterly geostrophic flow to create the notably favorable shear profiles present during the supercell outbreak. Together, the largely opposing near-surface ageostrophic component, accelerations occurring within the LLJ entrance region, and weak background geostrophic shear yielded strong deep-layer total vertical wind shear, while the strong southwesterly geostrophic flow effectively translated the highly curved ageostrophic hodographs into the first quadrant (typical of Southeast tornado environments; Markowski and Richardson 2006) and primarily supported the length and shape of the total wind hodographs in the middle to upper troposphere.

5. WRF simulations

a. Model configuration

To directly evaluate how latent processes contributed to the flow modifications discussed thus far, two simulations were conducted using version 4.1.2 of the WRF-ARW model (Skamarock et al. 2008): one configured using full model physics (LH), and one without latent heating or cooling (NOLH). Both simulations were initialized at 1800 UTC 26 April and run for 36 h to capture the outbreak entirely (Table 1). Initial conditions (ICs) for atmospheric and soil fields were obtained from the NCEP GFS 0.5° analysis valid at 1800 UTC 26 April, and lateral boundary conditions (BCs) were updated every 6 h using the corresponding GFS analyses.

Both simulations were run using a two-way nested grid configuration, with an outer domain of $\Delta x = \Delta y = 15$ km, and a convection-permitting inner domain of $\Delta x = \Delta y = 3$ km (Fig. 15). A stretched vertical grid comprising 70 levels below a 10-hPa model top was used. Identical physics parameterization schemes were employed for both simulations, except that the New Tiedtke cumulus scheme (Zhang et al. 2011) was only employed on the outer domain of the LH simulation. The Thompson microphysics scheme (Thompson et al. 2004, 2008) was used for both simulations, but no microphysics heating tendency was permitted in the NOLH simulation. The MYNN level-2.5, TKE-based PBL scheme was used in tandem with the MYNN surface layer scheme (Nakanishi and Niino 2006, 2009) and coupled Unified Noah LSM (Ek et al. 2003). Shortwave and longwave radiation were parameterized using the respective RRTMG schemes (Iacono et al. 2008). Radiative effects of clouds were permitted in both simulations.

b. Validity of simulation

The LH simulation was validated using the radar observations and RUC 1-h forecasts. Overall, the evolution of QLCS1 was well depicted, and a widespread region of strong convection had developed over Arkansas and Texas by 0000 UTC 27 April (cf. Figs. 1b and 16a). This convection quickly grew upscale into an expansive QLCS, but the southernmost bowing segment that resulted from the upscale growth of convection over eastern Texas and produced numerous tornadoes throughout the Southeast overnight was absent in the simulation[3] (cf. Figs. 1d–f and 16b,c). Although this discrepancy will inevitably influence any simulated modifications to the mesoscale environment over the Southeast, the adequate depiction of the initiation and rapid upscale growth of QLCS1 provides confidence that the LH simulation should reasonably portray the most significant upscale modifications described in section 4. However, QLCS2 developed ~4–5 h too early and ~150–200 km too far west in the LH simulation. The resultant environmental modifications from QLCS2—including the

[3]Cursory analyses from a convection-permitting ensemble of this event (not shown) suggest that this bowing segment had limited predictability.

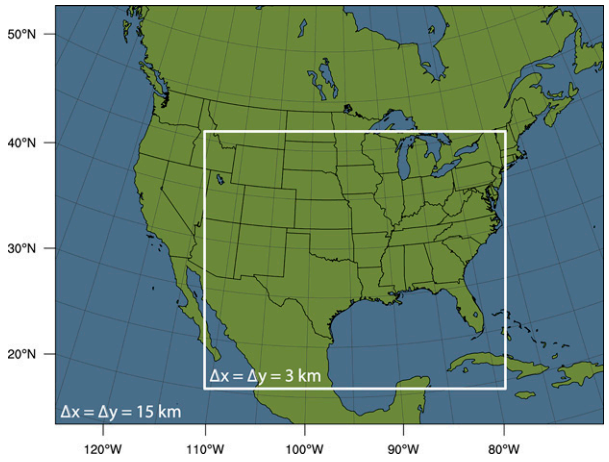

FIG. 15. The domain configuration used for the WRF-ARW simulations presented in section 4.

development and evolution of J_4, the intensification of the LLJ, and the system's interactions with SW_3 and J_1—and how they influenced conditions during the supercell outbreak were therefore depicted inaccurately. Thus, the WRF simulations are primarily used to further assess how QLCS1 altered the large-scale pattern and its own inflow environment. To mitigate the influence of QLCS2 on our analyses, we describe the flow modifications that had occurred by 0600 UTC 27 April—just before QLCS1 produced its first EF3 tornado (see Fig. 3 in Knupp et al. 2014). *We emphasize that the environmental conditions present at this time did not represent those during the supercell outbreak, which began ~12 h later.*

The LH simulation compared well to the corresponding RUC 1-h forecast at 0600 UTC 27 April in its depiction of the flow modifications occurring at both upper levels (particularly w.r.t. J_2; Figs. 17a,c) and low levels (particularly w.r.t. the LLJ; Figs. 17b,d). Specifically, simulated 250-hPa winds within J_2 were stronger than 130 kt over the Great Lakes region, and cross-isohypse ageostrophic flow, inferred accelerations, and mass divergence were apparent in the J_2 entrance region. At 850 hPa, the simulated LLJ intensified and advanced northward in conjunction with J_2, and a corridor of 55–70-kt winds extended into the Ohio Valley ahead of QLCS1 by 0600 UTC 27 April.

c. *Simulated flow modifications*

1) UPPER-LEVEL MODIFICATIONS

The environmental modifications stemming from QLCS1 were quantified by computing the difference between the LH and NOLH simulations (calculated as LH–NOLH) for several fields, including geopotential height and wind speed.[4] At 0600 UTC 27 April, 250-hPa height perturbations > 125 m were centered over southern Illinois (coincident with the QLCS1 stratiform region), while height perturbations > 50 m spanned much of the Midwest (Fig. 18a). This broad region of greater height values in the LH simulation signified the amplified downstream ridge and was centered within a perturbation anticyclone (Fig. 18b). The northern and western flanks of this anticyclone comprised wind speed perturbations of ~70–110 kt and ~70–100 kt and corresponded to J_2 and J_3, respectively. Additionally, relatively strong (~30–50 kt) easterly perturbations were evident along the southern flank, which opposed the background flow over the SGP (Fig. 17c) and supported enhanced decelerations within the J_1 exit region—consistent with our findings in section 4b.

Furthermore, QLCS1 had considerably altered the tropopause structure in the LH simulation. As depicted in Fig. 19, the 2-PVU surface within the NOLH simulation gradually sloped upward toward the east and was located at 9–11 km MSL within the vicinity of QLCS1. This surface had been lifted by ~3–4 km in the LH simulation, and a steepened tropopause and accompanying tropopause fold had developed behind QLCS1, which were absent in the NOLH simulation. The steepened tropopause and developing fold first appeared shortly after CI (owing to mass conservation and compensating subsidence; e.g., Phoenix et al. 2019) and progressively deepened with time as QLCS1 grew upscale (Figs. 19a,b). This secondary tropopause fold was not collocated with any appreciable positive PV tendency—that is, the high-PV values were not generated by diabatic processes occurring within QLCS1 (Figs. 19c,d). Rather, this high-PV intrusion comprised stratospheric air and resulted from sustained differential vertical motions occurring along the western periphery of QLCS1 and the formation of a strong underlying convective downdraft.

2) LOW-LEVEL MODIFICATIONS

At 850 hPa, the geopotential height and horizontal wind perturbations opposed those aloft—consistent with the expected hydrostatic and low-level PV response to diabatic processes occurring within QLCS1 (Figs. 18c,d). At 0600 UTC 27 April, a negative height perturbation < -60 m was centered over western Kentucky (nearly aligned with the greatest positive upper-level height perturbation), and a broad region of height difference values < -30 m spanned much of the Ohio Valley. This region of lower height values in the LH simulation coincided with a perturbation cyclonic circulation that was most pronounced at midlevels (not shown) in accordance with a positive PV anomaly that developed within QLCS1. The 850-hPa wind perturbations of 15–30 kt accompanied this circulation and augmented the background southerly flow throughout the QLCS1 inflow environment.

d. *Alterations to CAPE and CIN*

It is reasonable to conjecture that enhanced poleward advection of warm, moist air by the strengthened LLJ might yield greater CAPE (and reduced CIN) within the QLCS1 inflow environment. Difference fields for CAPE and CIN corresponding to the most-unstable parcel at 0600 UTC 27 April are shown in Figs. 20a and 20b. Conversely, CAPE decreases > 300 J kg^{-1} were widespread throughout the warm sector, and a corridor of CAPE decreases greater than 800 J kg^{-1} extended ~250 km ahead of the convective line beneath the

[4] The wind speed difference was calculated from the differences in u and v components as $[(\Delta u)^2 + (\Delta v)^2]^{1/2}$.

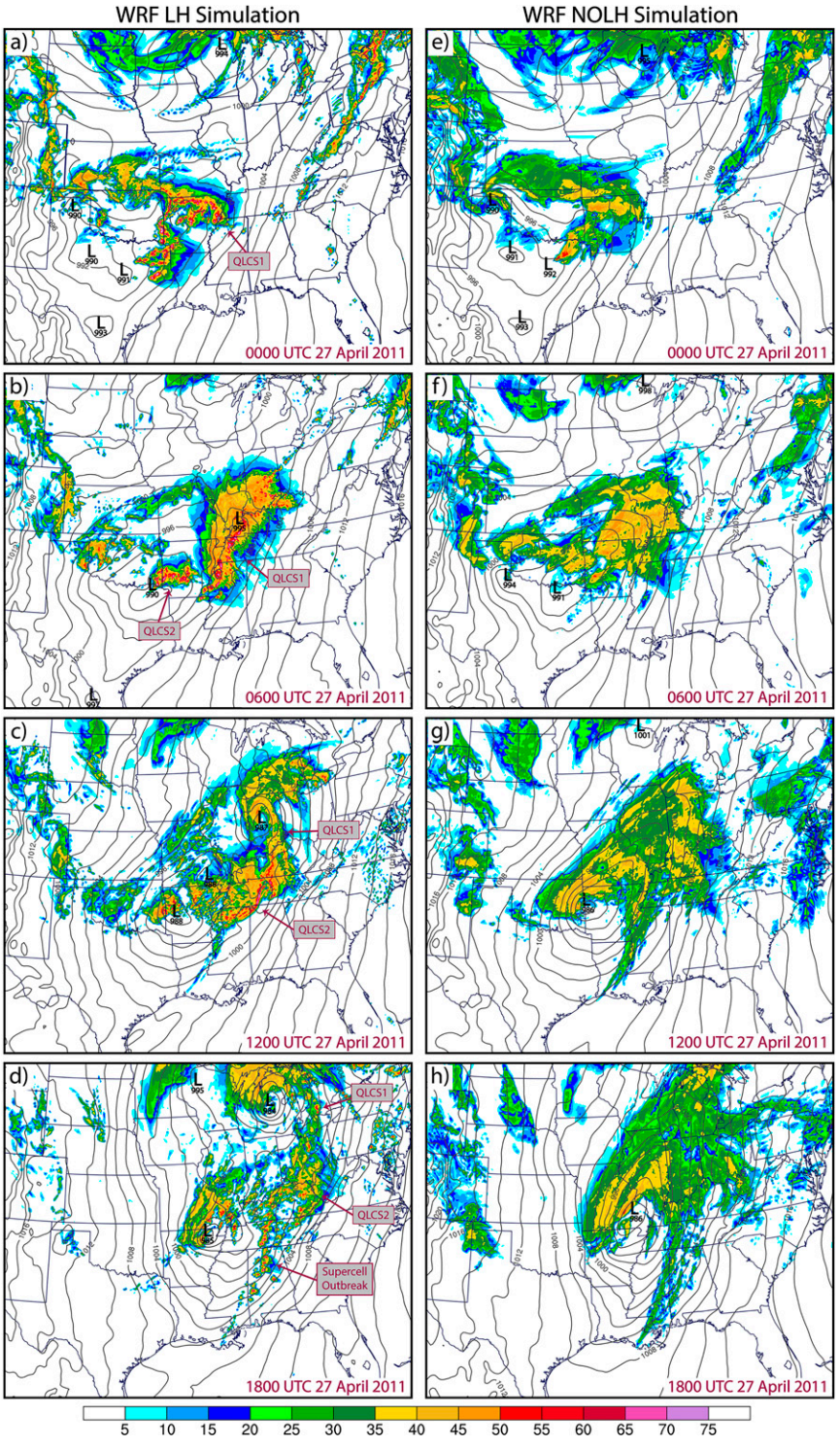

FIG. 16. Simulated radar reflectivity (shaded; dBZ) and SLP (gray contours; hPa) from the LH simulation at (a) 0000, (b) 0600, (c) 1200, and (d) 1800 UTC and the NOLH simulation at (e) 0000, (f) 0600, (g) 1200, and (h) 1800 UTC 27 Apr 2011. The reflectivity fields and SLP are shown on the 3-km inner domain and 15-km outer domain, respectively.

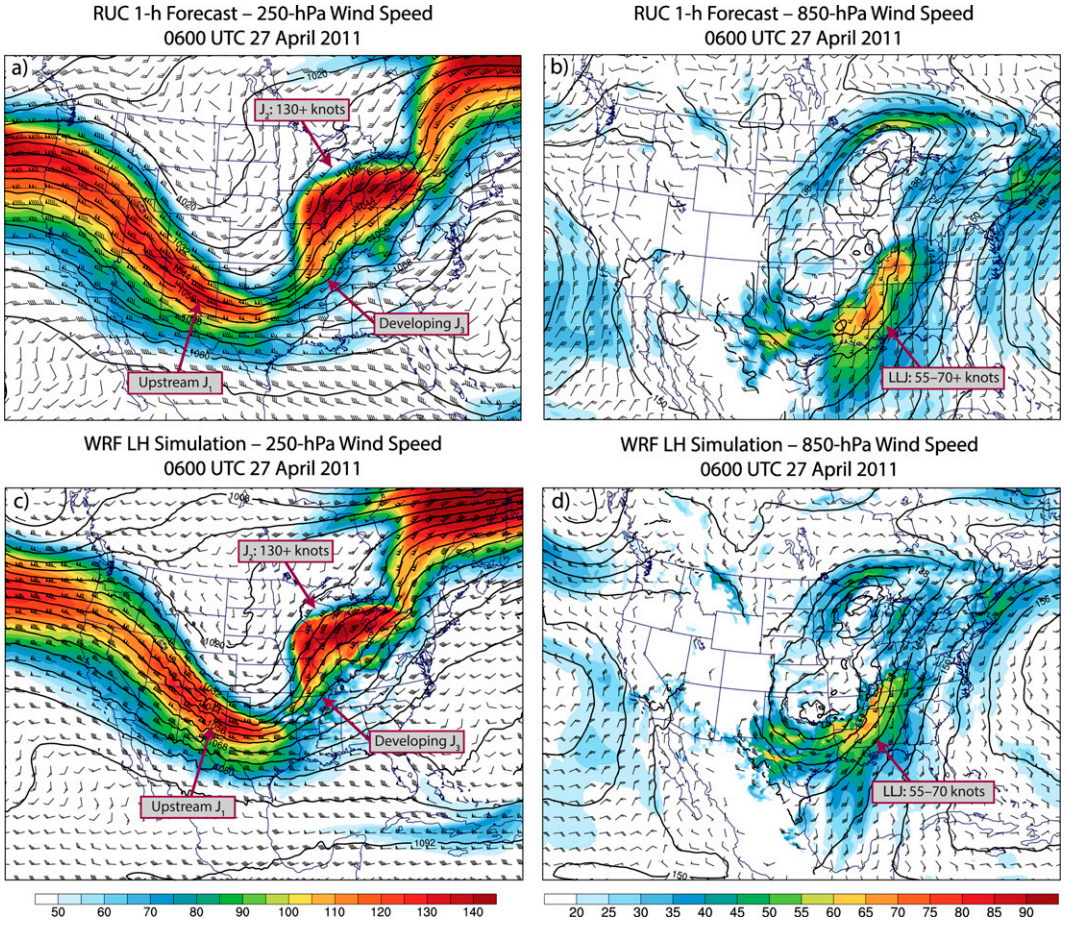

FIG. 17. Comparison of wind speed (shading; kt), geopotential height (contours; dam), and total winds (barbs; kt) valid at 0600 UTC 27 Apr as depicted by (top) the corresponding RUC 1-h forecast and (bottom) the WRF LH simulation at (a),(c) 250 hPa and at (b),(d) 850 hPa. The fields are shown on the 15-km outer domain.

anvil. The lateral extent of this diminished CAPE region quickly expanded away from QLCS1 following CI (not shown) and was due primarily to midlevel warming that resulted from deep-tropospheric subsidence—the manifestation of which is evident in Fig. 21. Although the LLJ had strengthened ahead of QLCS1, the adverse effects of subsidence warming were not offset by low-level advective processes owing to the presence of weak background thermal and moisture gradients. Consequently, the near-surface temperature and moisture profiles were essentially identical between the LH and NOLH simulations (Fig. 21). Thus, the net effect of latent heating was to diminish CAPE throughout the inflow environment—a finding consistent with previous studies (e.g., Lane and Reeder 2001; Adams-Selin and Johnson 2013).

Considerable mesoscale variability was evident in the CIN difference field, particularly in the environment ahead of QLCS1, where alternating bands of increased and decreased CIN values spanned from northern Mississippi into Kentucky (Fig. 20b). Overall, CIN was greater within the LH simulation—especially over Mississippi and Louisiana, where increases ranged from 30 to 60 J kg^{-1}. As CIN is primarily affected by thermodynamic modifications that manifest within the lower to middle troposphere, these increases were predominantly due to subsidence warming below ~700 hPa that strengthened a capping inversion beneath an elevated mixed layer in the LH simulation (Fig. 21a). Although this result might suggest that another important effect of latent processes was to yield thermodynamic conditions that were less conducive to cell regeneration and system longevity over the Southeast, we cannot affirm whether such a pronounced CIN enhancement would have occurred ahead of the southernmost bowing segment had it properly developed within the LH simulation.

e. *Alterations to vertical wind shear*

The vertical wind shear within the inflow environment was enhanced relative to the NOLH simulation. Difference fields of bulk wind difference (BWD) and SRH[5] calculated over the 0–1-km and 0–3-km layers are displayed in Figs. 20c–f. The greatest low-level shear increases occurred over

[5] All SRH calculations employed the right-moving supercell motion estimated using the Bunkers et al. (2000) technique, as this was used to compute SRH within the RUC model.

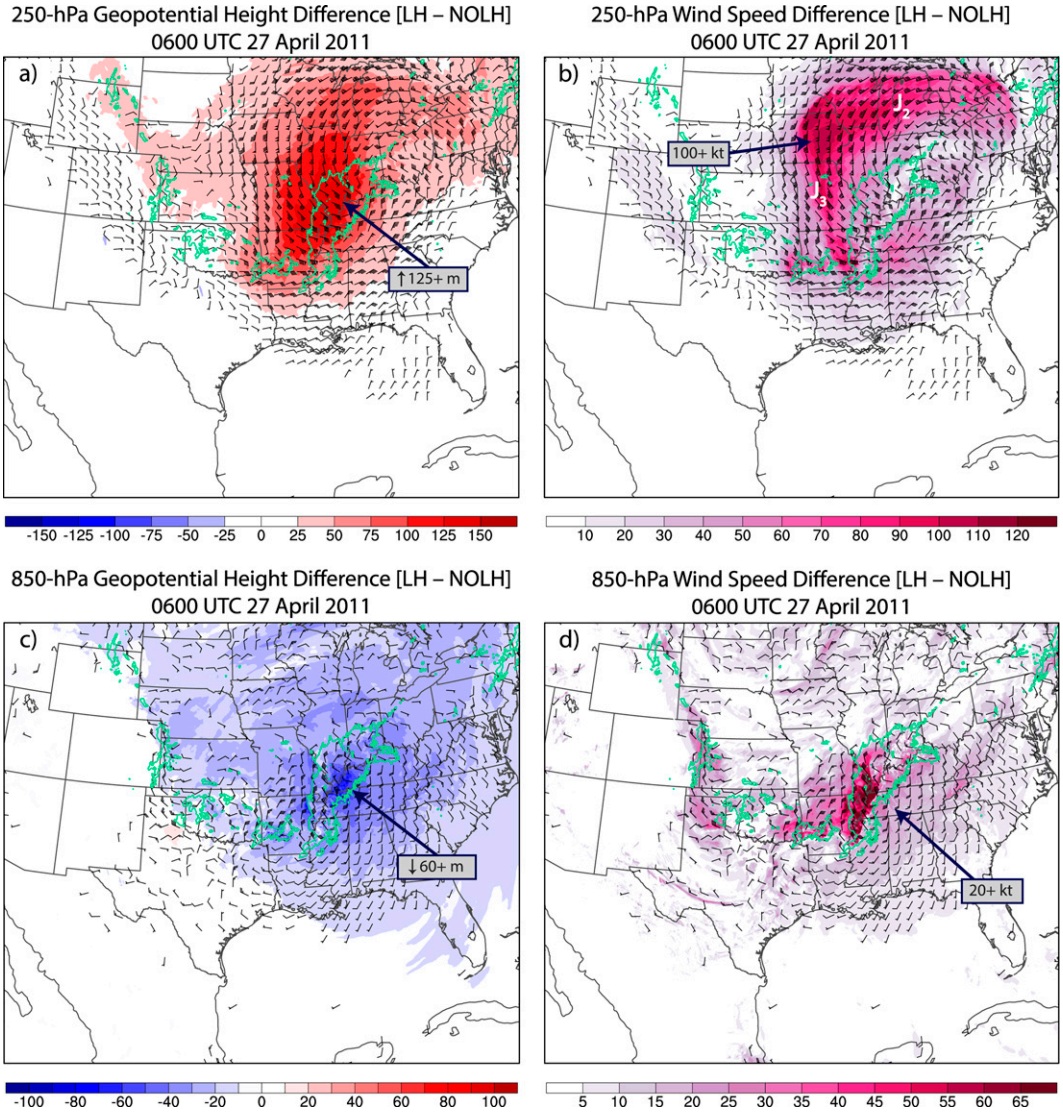

FIG. 18. Differences between the LH and NOLH WRF simulations of (a) 250-hPa geopotential height (shaded; m) and horizontal winds (barbs; kt), (b) 250-hPa wind speed (shaded; kt) and horizontal winds (barbs; kt), (c) 850-hPa geopotential height (shaded; m) and horizontal winds (barbs; kt), and (d) 850-hPa wind speed (shaded; kt) and horizontal winds (barbs; kt) at 0600 UTC 27 Apr. Simulated radar reflectivity = 35 dBZ from the LH simulation is displayed in all panels (green contours). All fields are shown on the 3-km inner domain.

the Ohio and Tennessee Valleys, where changes in 0–1-km and 0–3-km BWD magnitudes ranged over 10–30 kt and 15–40 kt, respectively. Such increases were related to the strengthened LLJ and perturbation cyclonic circulation (i.e., positive PV anomaly) that developed within the lower to middle troposphere. Low-level shear also increased over the Southeast—particularly just ahead of QLCS1—although the overall BWD enhancements were ~5–10 kt weaker in this region. The 0–1-km shear difference vector within the inflow environment was oriented approximately parallel to QLCS1—consistent with the findings of Part I in that the low-level shear profiles yielded considerable streamwise vorticity for inflowing parcels.

Unsurprisingly, the greatest increases in SRH and low-level shear were largely collocated, and a notable area of enhanced SRH—particularly when calculated over the 0–3-km layer—was situated east of a band of low-level cyclonic vorticity in Kentucky and Tennessee. Wind profiles from Nashville, Tennessee, and Huntsville, Alabama, indicate that these large SRH increases resulted from strengthened winds throughout the lowest ~5 km and significant changes in the hodograph shape (Figs. 21). SRH increases were also evident over the Southeast, and the hodograph from the LH simulation at Jackson, Mississippi, exhibited stronger vertical shear and greater low-level curvature than in the NOLH simulation, although the

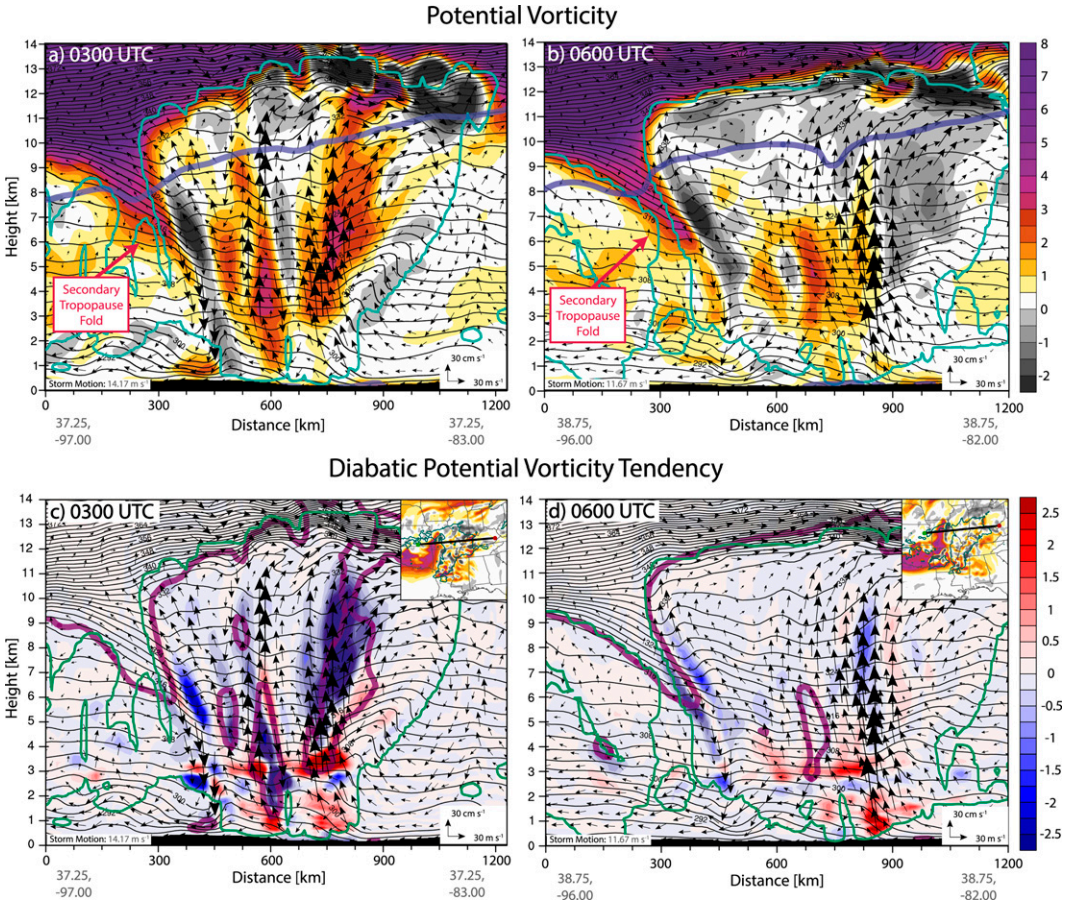

FIG. 19. At (a),(c) 0300 and (b),(d) 0600 UTC 27 Apr 2011, vertical cross sections of (top) PV from the LH simulation (shaded; PVU), potential temperature (gray contours; K), cloud boundary (cyan contour; defined as the sum of the cloud water, cloud ice, and snow mixing ratios = 0.001 g kg^{-1}), system-relative winds (vectors; scale shown on plots), and the 2-PVU contour from the NOLH simulation (blue) and (bottom) diabatic PV tendency (shaded; PVU h^{-1}), potential temperature (gray contours; K), cloud boundary (green contour), system-relative winds (vectors; scale shown on figure), and the 2-PVU contour from the LH simulation (purple). The cross-sectional paths, overlaid with 350-hPa PV (~8 km MSL) from the LH simulation, are shown in (c) and (d). Plotted fields are from the 15-km outer domain.

background shear and SRH values were already considerable. We note that the actual magnitude of differences over the Southeast may have been underrepresented by the WRF simulations because the observed QLCS extended ~400 km farther to the southwest at 0600 UTC 27 April. Comparisons with the RUC fields at Jackson suggest that the LH simulation underestimated 0–1-km BWD and 0–1-km SRH values by ~4 kt and ~120 m^2 s^{-2}, respectively (not shown). Overall, the WRF simulations indicate that *low-level shear and SRH increased markedly within the QLCS1 inflow environment and thus supported the system's notable severity and longevity—an upscale feedback effect.*

f. Accumulated modifications from latent heat release

We now discuss how the accumulated effects of latent heating occurring over 24 h modified the environment within the WRF simulation. Owing to 1) the absence of the southernmost bowing segment with QLCS1 in the LH simulation, 2) the premature development of QLCS2 and misrepresentation of its upscale modifications in the LH simulation, and 3) errors in the strength and forward progression of J_1 into the Southeast (i.e., too strong and too fast) in both WRF simulations, *the following analyses are not expected to replicate the environmental conditions during the supercell outbreak*, but rather serve to demonstrate how dramatically the simulated environment adjusted to prolonged convection. The composite radar reflectivity and SLP evolution for both simulations is shown in Fig. 16. Despite the lack of deep convection in the NOLH simulation, the precipitation distribution was generally comparable between the two simulations from 0000 to 1800 UTC 27 April. However, appreciable differences in the SLP field had arisen by 1200 UTC 27 April—particularly due to alterations in the evolution of L_1 and the formation of L_2

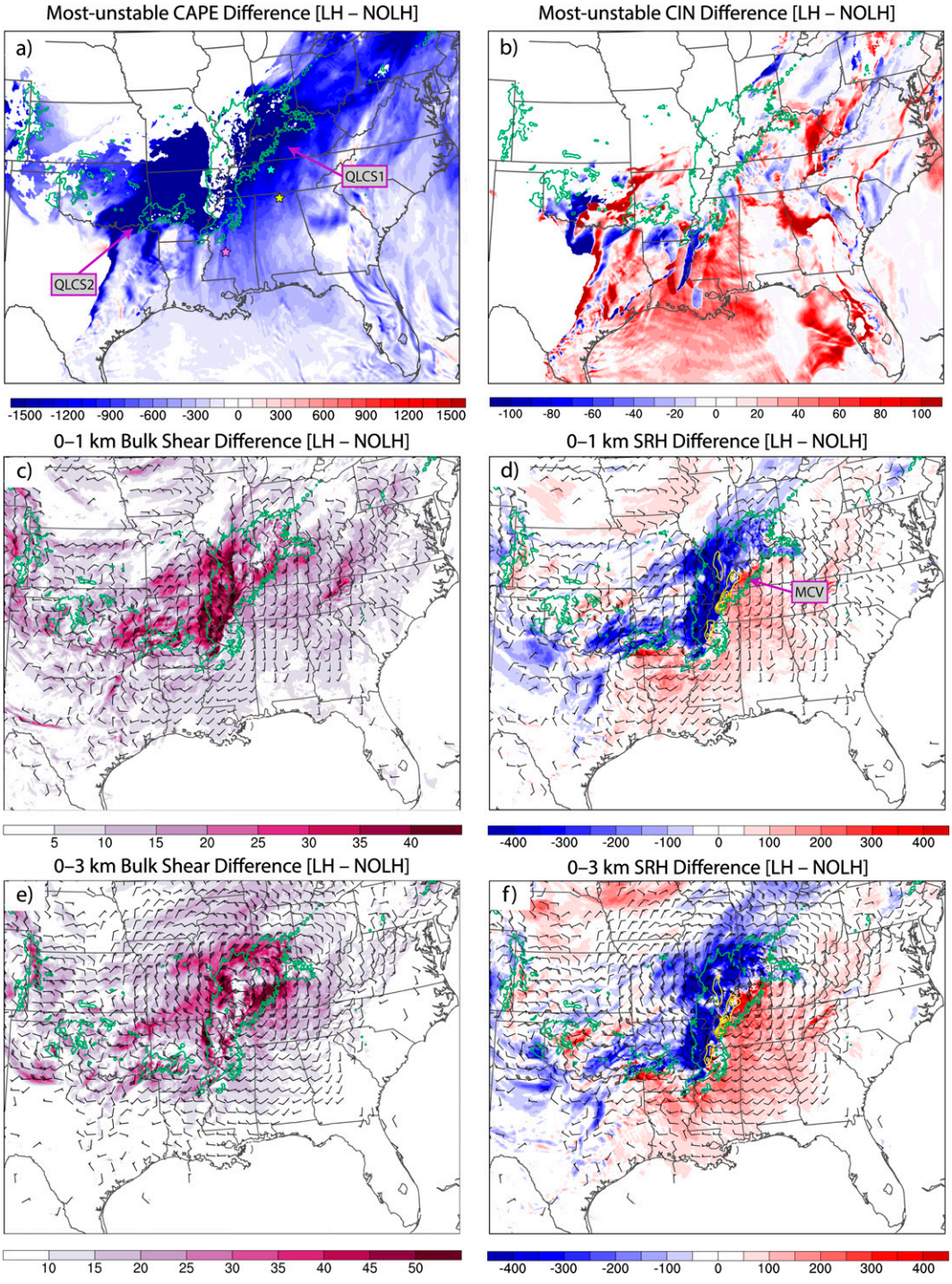

FIG. 20. Differences between the LH and NOLH WRF simulations of (a) CAPE (shaded; J kg^{-1}) and (b) CIN (shaded; J kg^{-1}) corresponding to the most-unstable parcel at 0600 UTC 27 Apr. CIN values are taken to be positive such that positive differences represent greater values of inhibition within the LH simulation. Also shown are differences in bulk wind shear (barbs; kt) and bulk wind shear magnitude (shaded; kt) calculated over the (c) 0–1- and (e) 0–3-km layers, and differences in bulk wind shear (barbs; kt) and SRH (shaded; m^2 s^{-2}) calculated over the (d) 0–1- and (f) 0–3 km layers at 0600 UTC 27 Apr 2011. Simulated radar reflectivity = 35 dBZ from the LH simulation is displayed in all panels (green contours). PV averaged within the 900–700-hPa layer (yellow contours; every 2 PVU ≥ 2 PVU) is displayed in (d) and (f). All fields except for PV are shown on the 3-km inner domain.

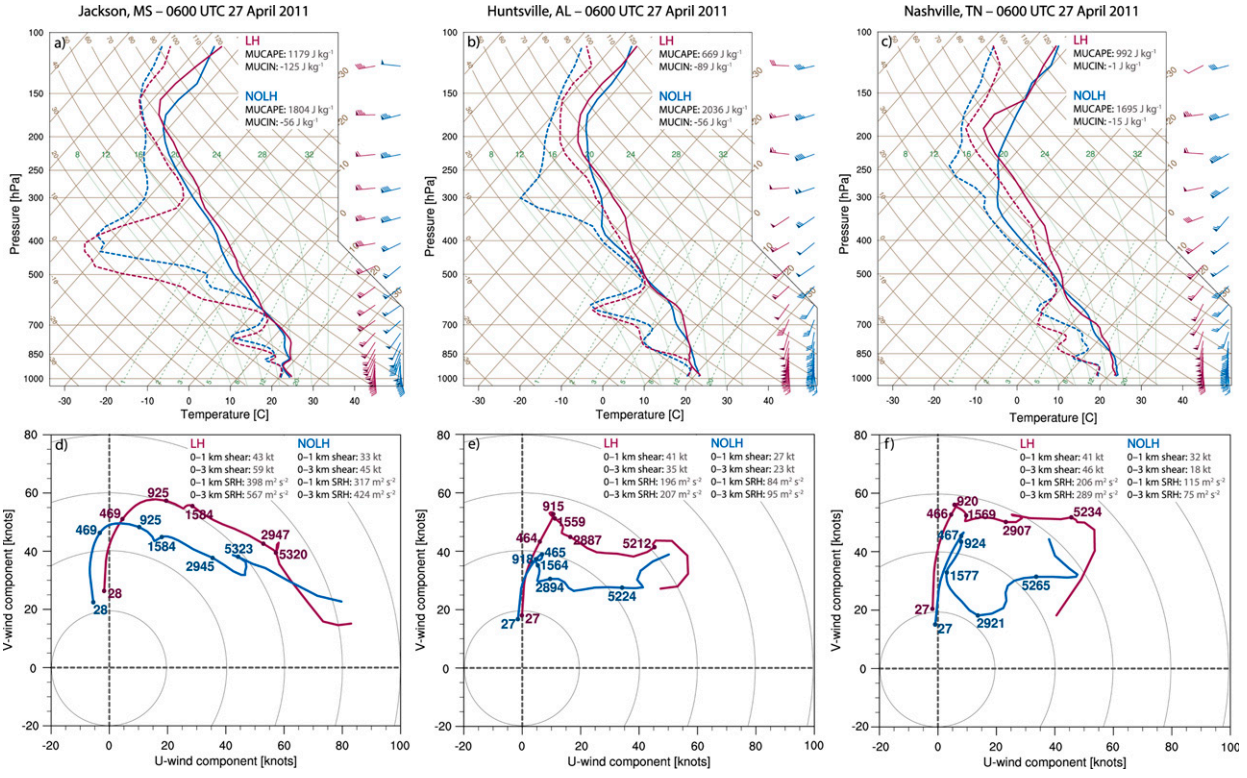

FIG. 21. Soundings and corresponding hodographs (displayed below 8 km AGL) from the LH (magenta) and NOLH (blue) WRF simulations valid at 0600 UTC 27 Apr 2011 for the locations of (a),(d) Jackson, MS; (b),(e) Huntsville, AL; and (c),(f) Nashville, TN. The locations of Jackson, Huntsville, and Nashville are denoted by the pink, yellow, and cyan markers in Fig. 20a, respectively.

over the Midwest in the LH simulation. Notably, L_2 was completely absent in the NOLH simulation, solidifying that latent processes and upscale modifications were essential for cyclogenesis to occur with SW_2.

Considerable differences in the simulated baroclinic environment were evident at 1800 UTC 27 April (Fig. 22). At midlevels, SW_2 had become amplified over the Great Lakes region in the LH simulation (Fig. 22a), whereas a distinct cyclonic perturbation with SW_2 was absent in the NOLH simulation (Figs. 22d,g). Consequently, the NOLH simulation featured a negatively tilted and highly diffluent midlevel baroclinic wave supportive of broad forcing for ascent over the Midwest, while the baroclinic wave in the LH simulation exhibited an elongated structure with limited downstream diffluence owing to the added presence of SW_2. Differences in the low-level kinematic and thermodynamic environments were also apparent and resulted both directly from the QLCSs (e.g., production of cool surface outflow) and indirectly (e.g., modifications to the baroclinic wave structure and thus dynamical forcing for low-level height falls and cyclogenesis). The NOLH simulation featured an elongated trough that extended northward from L_3 into the Great Lakes region and supported a highly amplified warm sector comprising uninterrupted southerly flow with an embedded LLJ that was actively strengthening beneath the J_1 exit region at this time (Figs. 22e,f). In contrast, L_3 was deeper and more contracted in scale in the LH simulation (Figs. 22b,c), and the added height perturbations accompanying L_2 and its appendage trough—which extended southwestward into the Gulf of Mexico and was collocated with a perturbation cyclonic wind (Fig. 22h)—promoted more veered southwesterly low-level flow over the Southeast. Moreover, two LLJ maxima had formed in association with L_2 and L_3, and the southern maximum (which comprised 60–70-kt winds—slower than in the RUC, primarily due to the misrepresentation of J_4) was bounded to the north by the residual cold pool (Figs. 22b,c). Overall, the structure of the thermal wave was significantly modified by convection in the LH simulation, with differences evident in the baroclinity and position of surface fronts (e.g., the cold front in Mississippi) and the confinement of the "warm sector" to the south of the effective warm front (Fig. 22i).

6. Summary and discussion

Herein we evaluated the environmental modifications produced by two successive QLCSs during the 26–27 April 2011 multiepisode tornado outbreak. Overall, QLCS1 drastically altered the large-scale pattern and induced flow modifications that contributed to its upscale growth and notable severity, while QLCS2 modified the mesoscale environment and enhanced the shear profiles over the Southeast prior to the supercell outbreak. Collectively, these multiscale modifications

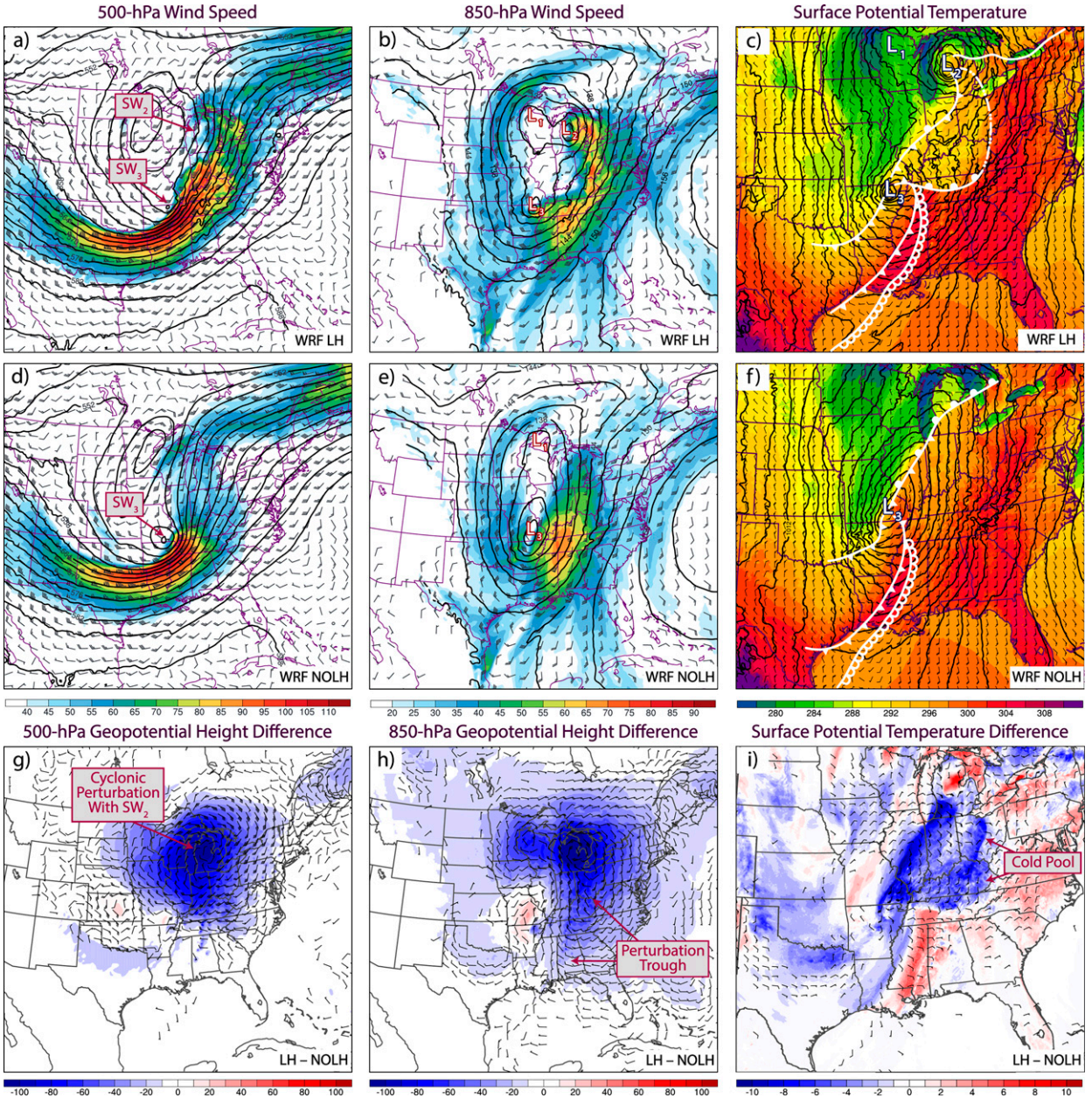

FIG. 22. Comparison of wind speed (shading; kt), geopotential height (contours; dam), and total winds (barbs; kt) valid at 1800 UTC 27 Apr from the LH simulation at (a) 500 and (b) 850 hPa and NOLH simulation at (d) 500 and (e) 850 hPa. Also shown are difference fields of geopotential height (shaded; m) and horizontal winds (barbs; kt) at (g) 500 and (h) 850 hPa. Corresponding analyses of 2-m potential temperature (shaded; K), SLP (contours; hPa), 10-m winds (barbs; kt), and manually analyzed surface fronts are shown for the (c) LH and (f) NOLH simulations. (i) Difference fields of surface potential temperature (shaded; K) and 10-m winds (barbs; kt). The upper-level fields are shown on the 15-km outer domain, and the surface fields are shown on the 3-km inner domain.

yielded conditions that likely enhanced the severity of convection during the outbreak.

Specific and noteworthy findings were as follows:

- Following CI associated with QLCS1 on the evening of 26 April, upper-level geopotential heights increased downstream from SW_2, which amplified the flow curvature and induced dynamical imbalance. Over eastern Texas, convection interrupted the upper-level jet exit region and yielded greater parcel decelerations and a stronger thermally indirect transverse circulation. Over Arkansas, widespread convection rapidly sharpened the preexisting upper-level PV gradient that was established in the wake of SW_1 (via diabatic PV erosion and negative PV advection by strong divergent outflow) and consequently promoted the downstream formation of J_2.

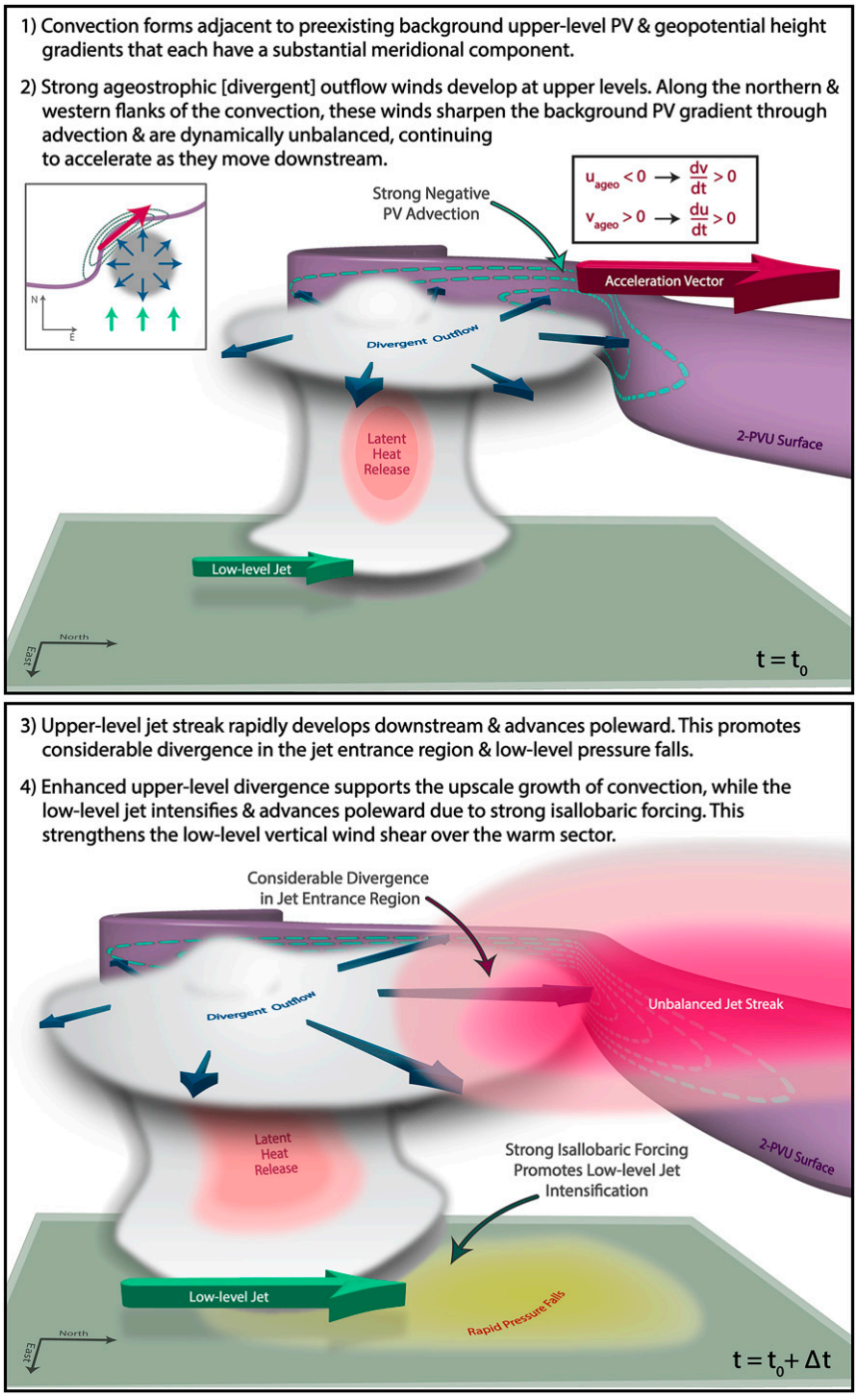

FIG. 23. Schematic summarizing how convection interacting with background PV and geopotential height gradients along the southeastern flank of an amplified upper-level trough can promote the development of an unbalanced upper-level jet streak that rapidly advances poleward, aiding in the upscale growth of convection and yielding considerable intensification of the LLJ and low-level shear within the warm sector.

- The J_2 entrance region was dynamically unbalanced and highly divergent, which facilitated QLCS1's upscale growth as J_2 rapidly strengthened and advanced poleward overnight. This evolution promoted downstream ridge amplification and reduced the wavelength and eastward progression of the large-scale pattern. Moreover, J_2 was accompanied by an isallobaric response that rapidly intensified the LLJ ahead of QLCS1.

- The upper-level height and PV gradients strengthened to the west of QLCS1 following its upscale growth and promoted the formation of J_3 by 0600 UTC 27 April. Furthermore, differential vertical motions and sustained midlevel subsidence induced a tropopause fold behind QLCS1, which did not form in the absence of latent heating. This secondary tropopause fold was directly attributable to the development and upscale growth of convection near a preexisting PV gradient and prolonged environmental modifications arising from this convection.
- Cyclogenesis occurred along the quasi-stationary front behind QLCS1 as the secondary tropopause fold and amplified SW_2 interacted with a prominent low- to midlevel PV anomaly. L_2 did not develop in the absence of latent heating and was therefore a direct consequence of the upscale modifications from QLCS1. The height perturbations accompanying L_2 and its associated trough supported more veered low-level flow over the Southeast during the afternoon. Moreover, continued amplification of SW_2 diminished the large-scale flow curvature downstream from the upper-level trough and helped establish strong southwesterly flow aloft over the Southeast.
- Using WRF simulations configured with and without latent heating, we evaluated whether the thermodynamic and kinematic environmental modifications arising from QLCS1 may have furthered its longevity and severity. In the LH simulation, low-level wind shear increased throughout the inflow environment, and the 0–1-km shear difference vector was oriented nearly parallel to QLCS1 at 0600 UTC 27 April—supportive of the strong line-parallel shear emphasized in Part I. SRH also increased in conjunction with greater shear and hodograph curvature. Therefore, QLCS1 provided more favorable kinematic conditions for the production of severe convective hazards (e.g., damaging winds and tornadoes)—an upscale feedback effect that likely enhanced its own severity. Conversely, CAPE decreased throughout the environment in the LH simulation, predominantly due to warming aloft congruent with deep-tropospheric subsidence and mass conservation. However, coherent CIN increases were primarily confined to the south of QLCS1, with alternating mesoscale regions of increased and decreased CIN found within the immediate inflow environment.
- QLCS2 was accompanied by a meso-α-scale region of upper-level height rises and midlevel warming that enhanced the mesoscale flow curvature and baroclinity ahead of SW_3 during the morning of 27 April and promoted the generation of J_4 downstream over the Midwest. The right-entrance region of J_4 was unbalanced and characterized by considerable upper-level divergence. Furthermore, the J_1 exit region was split into two branches around QLCS2, and the southern branch contributed to the strong deep-layer shear present over the Southeast during the afternoon. This flow disruption—coupled with the rapid strengthening of J_4—yielded an isallobaric response that further intensified the LLJ ahead of SW_3 and established a regional maximum in low-level wind speed (and accordingly low-level shear) over northern Mississippi and Alabama during the supercell outbreak.
- The respective contributions of geostrophic and ageostrophic motions to the total wind hodographs over the Southeast at the beginning of the supercell outbreak were evaluated. The geostrophic hodographs all depicted strong southwesterly flow but overall weak vertical wind shear that alone would not have supported a prolific tornado outbreak. In contrast, the highly curved hodographs and strength of the vertical wind shear throughout the lower to middle troposphere were due almost entirely to the ageostrophic wind profile, which veered appreciably with height and resulted from a combination of frictional effects, flow curvature, and—of particular importance—strong accelerations within the LLJ entrance region. Thus, ageostrophic motions were absolutely essential to creating the highly favorable shear profiles present during the prolific afternoon supercell outbreak.
- Of notable importance in this event was the development and rapid strengthening of convectively forced jet streaks downstream from the upper-level trough—specifically, the formation of J_2 with QLCS1 and J_4 with QLCS2. Both jet streaks resulted from convection intruding upon preexisting geopotential height and PV gradients that were established in the wake of a preceding shortwave trough and thus had a substantial meridional component. Consequently, the upper-level outflow that developed along the northern and western flanks of the QLCSs became dynamically unbalanced, yielding strong accelerations as these outflow jets quickly advanced poleward with time—analogous to the poleward momentum surges described by Rowe and Hitchman (2016). This unique evolution augmented the strength of the LLJ and vertical wind shear over the warm sector throughout the outbreak and is schematized in Fig. 23.

This research was motivated by the need for improved physical understanding and forecasts of tornado outbreaks in the Southeast, which are generally plagued by poor mesoscale predictability and frequently occur during prolonged periods of convection. Herein we demonstrated that two QLCSs provided a complex array of upscale environmental modifications prior to the prolific afternoon supercell tornado outbreak on 27 April. Unfortunately, errors within the WRF simulations—particularly with regard to the evolution of QLCS2 and J_4—preclude us from fully understanding how these upscale modifications affected the supercell outbreak. To our knowledge, the significance of upscale feedbacks in multiepisode severe outbreaks has not been previously evaluated although such events are notoriously challenging for forecasters. We hope that greater attention is drawn to this matter—especially within the forecasting and numerical modeling communities—as simulated environmental modifications are expected to be highly sensitive to the timing and location of CI, the extent and strength of convection, the specific representation of latent processes (i.e., model configuration), and the degree to which the convection interacts with the greater baroclinic environment.

Acknowledgments. This work was supported by NOAA/NSSL VORTEX-SE funding and the NSF/NCAR ASP Graduate Visitor Fellowship. Analyses and simulations were conducted using the OU/OSCER Schooner and

NCAR/CISL Cheyenne supercomputers. Kiel Ortega provided the MYRORSS radar composites, and Pat Skinner provided code to compute various WRF diagnostics. This work has benefited from discussions with Lance Bosart, Jimmy Correia, Chris Davis, Tom Galarneau, Tony Lyza, Erik Rasmussen, Glen Romine, Rich Rotunno, Ryan Sobash, Stan Trier, and Morris Weisman and the thoughtful comments from three anonymous reviewers.

Data availability statement. RUC forecasts were obtained from the NOAA/NCEI Operational Model Archive and Distribution System database (https://www.ncdc.noaa.gov/data-access/model-data). GFS analyses were acquired from NCAR's Research Data Archive (https://rda.ucar.edu/datasets/ds084.6). Radar imagery was obtained from the Multi-Year Reanalysis of Remotely Sensed Storms archive (https://osf.io/8f4v2/). NOAA wind profiler observations were obtained from the MADIS archive. Satellite observations were obtained from NOAA's Comprehensive Large Array-data Stewardship System (https://www.avl.class.noaa.gov/). The WRF-ARW output can be made available upon request.

REFERENCES

Adams-Selin, R. D., and R. H. Johnson, 2013: Examination of gravity waves associated with the 13 March 2003 bow echo. *Mon. Wea. Rev.*, **141**, 3735–3756, https://doi.org/10.1175/MWR-D-12-00343.1.

Anthes, R. A., Y.-H. Kuo, S. G. Benjamin, and Y.-F. Li, 1982: The evolution of the mesoscale environment of severe local storms: Preliminary modeling results. *Mon. Wea. Rev.*, **110**, 1187–1213, https://doi.org/10.1175/1520-0493(1982)110<1187:TEOTME>2.0.CO;2.

Archambault, H. M., L. F. Bosart, D. Keyser, and J. M. Cordeira, 2013: A climatological analysis of the extratropical flow response to recurving western North Pacific tropical cyclones. *Mon. Wea. Rev.*, **141**, 2325–2346, https://doi.org/10.1175/MWR-D-12-00257.1.

Atallah, E. H., and L. F. Bosart, 2003: The extratropical transition and precipitation distribution of Hurricane Floyd (1999). *Mon. Wea. Rev.*, **131**, 1063–1081, https://doi.org/10.1175/1520-0493(2003)131<1063:TETAPD>2.0.CO;2.

Banacos, P. C., and H. B. Bluestein, 2004: Hodograph variability within analytically modeled, synoptic-scale, baroclinic systems. *Mon. Wea. Rev.*, **132**, 1448–1461, https://doi.org/10.1175/1520-0493(2004)132<1448:HVWAMS>2.0.CO;2.

Benjamin, S. G., G. A. Grell, J. M. Brown, T. G. Smirnova, and R. Bleck, 2004a: Mesoscale weather prediction with the RUC hybrid isentropic–terrain-following coordinate model. *Mon. Wea. Rev.*, **132**, 473–494, https://doi.org/10.1175/1520-0493(2004)132<0473:MWPWTR>2.0.CO;2.

——, and Coauthors, 2004b: An hourly assimilation–forecast cycle: The RUC. *Mon. Wea. Rev.*, **132**, 495–518, https://doi.org/10.1175/1520-0493(2004)132<0495:AHACTR>2.0.CO;2.

Bretherton, C. S., and P. K. Smolarkiewicz, 1989: Gravity waves, compensating subsidence and detrainment around cumulus clouds. *J. Atmos. Sci.*, **46**, 740–759, https://doi.org/10.1175/1520-0469(1989)046<0740:GWCSAD>2.0.CO;2.

Brooks, H. E., and R. B. Wilhelmson, 1993: Hodograph curvature and updraft intensity in numerically modeled supercells. *J. Atmos. Sci.*, **50**, 1824–1833, https://doi.org/10.1175/1520-0469(1993)050<1824:HCAUII>2.0.CO;2.

Bunkers, M. J., B. A. Klimowski, J. W. Zeitler, R. L. Thompson, and M. L. Weisman, 2000: Predicting supercell motion using a new hodograph technique. *Wea. Forecasting*, **15**, 61–79, https://doi.org/10.1175/1520-0434(2000)015<0061:PSMUAN>2.0.CO;2.

——, M. R. Hjelmfelt, and P. L. Smith, 2006: An observational examination of long-lived supercells. Part I: Characteristics, evolution, and demise. *Wea. Forecasting*, **21**, 673–688, https://doi.org/10.1175/WAF949.1.

Charney, J., 1955: The use of the primitive equations of motion in numerical prediction. *Tellus*, **7**, 22–26, https://doi.org/10.3402/tellusa.v7i1.8772.

Chasteen, M. B., and S. E. Koch, 2021: Multiscale aspects of the 26–27 April 2011 tornado outbreak. Part I: Outbreak chronology and environmental evolution. *Mon. Wea. Rev.*, **150**, 309–335, https://doi.org/10.1175/MWR-D-21-0013.1.

Coffer, B. E., M. D. Parker, R. L. Thompson, B. T. Smith, and R. E. Jewell, 2019: Using near-ground storm relative helicity in supercell tornado forecasting. *Wea. Forecasting*, **34**, 1417–1435, https://doi.org/10.1175/WAF-D-19-0115.1.

Cotton, W. R., M.-S. Lin, R. L. McAnelly, and C. J. Tremback, 1989: A composite model of mesoscale convective complexes. *Mon. Wea. Rev.*, **117**, 765–783, https://doi.org/10.1175/1520-0493(1989)117<0765:ACMOMC>2.0.CO;2.

Davies-Jones, R., 1984: Streamwise vorticity: The origin of updraft rotation in supercell storms. *J. Atmos. Sci.*, **41**, 2991–3006, https://doi.org/10.1175/1520-0469(1984)041<2991:SVTOOU>2.0.CO;2.

Davis, C. A., and K. A. Emanuel, 1991: Potential vorticity diagnostics of cyclogenesis. *Mon. Wea. Rev.*, **119**, 1929–1953, https://doi.org/10.1175/1520-0493(1991)119<1929:PVDOC>2.0.CO;2.

——, and M. L. Weisman, 1994: Balanced dynamics of mesoscale vortices produced in simulated convective systems. *J. Atmos. Sci.*, **51**, 2005–2030, https://doi.org/10.1175/1520-0469(1994)051<2005:BDOMVP>2.0.CO;2.

Dean, A., and R. Schneider, 2008: Forecast challenges at the NWS Storm Prediction Center relating to the frequency of favorable severe storm environments. *24th Conf. on Severe Local Storms*, Charleston, SC, Amer. Meteor. Soc., 9A.2, https://ams.confex.com/ams/24SLS/techprogram/paper_141743.htm.

Dickinson, M. J., L. F. Bosart, W. E. Bracken, G. J. Hakim, D. M. Schultz, M. A. Bedrick, and K. R. Tyle, 1997: The March 1993 superstorm cyclogenesis: Incipient phase synoptic-and convective-scale flow interaction and model performance. *Mon. Wea. Rev.*, **125**, 3041–3072, https://doi.org/10.1175/1520-0493(1997)125<3041:TMSCIP>2.0.CO;2.

Doswell, C. A., 1991: A review for forecasters on the application of hodographs to forecasting severe thunderstorms. *Natl. Wea. Dig.*, **16**, 2–16.

——, and L. F. Bosart, 2001: Extratropical synoptic-scale processes and severe convection. *Severe Convective Storms*, C. A. Doswell, Ed., Springer, 27–69.

Duchon, C. E., 1979: Lanczos filtering in one and two dimensions. *J. Appl. Meteor.*, **18**, 1016–1022, https://doi.org/10.1175/1520-0450(1979)018<1016:LFIOAT>2.0.CO;2.

Ek, M., K. Mitchell, Y. Lin, E. Rogers, P. Grunmann, V. Koren, G. Gayno, and J. Tarpley, 2003: Implementation of Noah land surface model advances in the National Centers for Environmental Prediction operational mesoscale Eta model. *J. Geophys. Res.*, **108**, 8851, https://doi.org/10.1029/2002JD003296.

Fritsch, J., and R. Maddox, 1981: Convectively driven mesoscale weather systems aloft. Part I: Observations. *J. Appl. Meteor.*, **20**, 9–19, https://doi.org/10.1175/1520-0450(1981)020<0009:CDMWSA>2.0.CO;2.

Galway, J. G., and A. Pearson, 1981: Winter tornado outbreaks. *Mon. Wea. Rev.*, **109**, 1072–1080, https://doi.org/10.1175/1520-0493(1981)109<1072:WTO>2.0.CO;2.

Garner, J., 2012: Environments of significant tornadoes occurring within the warm sector versus those occurring along surface baroclinic boundaries. *Electron. J. Severe Storms Meteor.*, **7** (5), https://www.spc.noaa.gov/publications/garner/ejssm.pdf.

Gold, D. A., and J. W. Nielsen-Gammon, 2008: Potential vorticity diagnosis of the severe convective regime. Part IV: Comparison with modeling simulations of the Moore tornado outbreak. *Mon. Wea. Rev.*, **136**, 1612–1629, https://doi.org/10.1175/2007MWR2093.1.

Grams, C. M., and H. M. Archambault, 2016: The key role of diabatic outflow in amplifying the midlatitude flow: A representative case study of weather systems surrounding western North Pacific extratropical transition. *Mon. Wea. Rev.*, **144**, 3847–3869, https://doi.org/10.1175/MWR-D-15-0419.1.

——, S. C. Jones, C. A. Davis, P. A. Harr, and M. Weissmann, 2013: The impact of Typhoon Jangmi (2008) on the midlatitude flow. Part I: Upper-level ridgebuilding and modification of the jet. *Quart. J. Roy. Meteor. Soc.*, **139**, 2148–2164, https://doi.org/10.1002/qj.2091.

Guyer, J. L., D. A. Imy, and A. Kis, 2006: Cool season significant (F2-F5) tornadoes in the Gulf Coast states. *23rd Conf. on Severe Local Storms*, St. Louis, MO, Amer. Meteor. Soc., 4.2.

Hamill, T. M., R. S. Schneider, H. E. Brooks, G. S. Forbes, H. B. Bluestein, M. Steinberg, D. Meléndez, and R. M. Dole, 2005: The May 2003 extended tornado outbreak. *Bull. Amer. Meteor. Soc.*, **86**, 531–542, https://doi.org/10.1175/BAMS-86-4-531.

Hoskins, B. J., 1975: The geostrophic momentum approximation and the semi-geostrophic equations. *J. Atmos. Sci.*, **32**, 233–242, https://doi.org/10.1175/1520-0469(1975)032<0233:TGMAAT>2.0.CO;2.

Hoxit, L. R., and C. F. Chappell, 1975: Tornado outbreak of April 3–4, 1974: Synoptic analysis. NOAA Tech. Rep. ERL 338-APCL 37, 48 pp.

Iacono, M. J., J. S. Delamere, E. J. Mlawer, M. W. Shephard, S. A. Clough, and W. D. Collins, 2008: Radiative forcing by long-lived greenhouse gases: Calculations with the AER radiative transfer models. *J. Geophys. Res.*, **113**, D13103, https://doi.org/10.1029/2008JD009944.

Kaplan, M. L., Y.-L. Lin, D. W. Hamilton, and R. A. Rozumalski, 1998: The numerical simulation of an unbalanced jetlet and its role in the Palm Sunday 1994 tornado outbreak in Alabama and Georgia. *Mon. Wea. Rev.*, **126**, 2133–2165, https://doi.org/10.1175/1520-0493(1998)126<2133:TNSOAU>2.0.CO;2.

Keyser, D., and M. Shapiro, 1986: A review of the structure and dynamics of upper-level frontal zones. *Mon. Wea. Rev.*, **114**, 452–499, https://doi.org/10.1175/1520-0493(1986)114<0452:AROTSA>2.0.CO;2.

——, and D. R. Johnson, 1984: Effects of diabatic heating on the ageostrophic circulation of an upper tropospheric jet streak. *Mon. Wea. Rev.*, **112**, 1709–1724, https://doi.org/10.1175/1520-0493(1984)112<1709:EODHOT>2.0.CO;2.

Knupp, K. R., and Coauthors, 2014: Meteorological overview of the devastating 27 April 2011 tornado outbreak. *Bull. Amer. Meteor. Soc.*, **95**, 1041–1062, https://doi.org/10.1175/BAMS-D-11-00229.1.

Koch, S. E., and P. B. Dorian, 1988: A mesoscale gravity wave event observed during CCOPE. Part III: Wave environment and probable source mechanisms. *Mon. Wea. Rev.*, **116**, 2570–2592, https://doi.org/10.1175/1520-0493(1988)116<2570:AMGWEO>2.0.CO;2.

——, D. Hamilton, D. Kramer, and A. Langmaid, 1998: Mesoscale dynamics in the Palm Sunday tornado outbreak. *Mon. Wea. Rev.*, **126**, 2031–2060, https://doi.org/10.1175/1520-0493(1998)126<2031:MDITPS>2.0.CO;2.

Kocin, P. J., L. W. Uccellini, and R. A. Petersen, 1986: Rapid evolution of a jet streak circulation in a pre-convective environment. *Meteor. Atmos. Phys.*, **35**, 103–138, https://doi.org/10.1007/BF01026169.

Kuo, Y.-H., M. Shapiro, and E. G. Donall, 1991: The interaction between baroclinic and diabatic processes in a numerical simulation of a rapidly intensifying extratropical marine cyclone. *Mon. Wea. Rev.*, **119**, 368–384, https://doi.org/10.1175/1520-0493(1991)119<0368:TIBBAD>2.0.CO;2.

Lackmann, G. M., 2002: Cold-frontal potential vorticity maxima, the low-level jet, and moisture transport in extratropical cyclones. *Mon. Wea. Rev.*, **130**, 59–74, https://doi.org/10.1175/1520-0493(2002)130<0059:CFPVMT>2.0.CO;2.

Lane, T. P., and M. J. Reeder, 2001: Convectively generated gravity waves and their effect on the cloud environment. *J. Atmos. Sci.*, **58**, 2427–2440, https://doi.org/10.1175/1520-0469(2001)058<2427:CGGWAT>2.0.CO;2.

Maddox, R. A., 1980: Mesoscale convective complexes. *Bull. Amer. Meteor. Soc.*, **61**, 1374–1387, https://doi.org/10.1175/1520-0477(1980)061<1374:MCC>2.0.CO;2.

——, and C. A. Doswell, 1982: An examination of jet stream configurations, 500 mb vorticity advection, and low-level thermal advection patterns during extended periods of intense convection. *Mon. Wea. Rev.*, **110**, 184–197, https://doi.org/10.1175/1520-0493(1982)110<0184:AEOJSC>2.0.CO;2.

——, L. R. Hoxit, and C. F. Chappell, 1980: A study of tornadic thunderstorm interactions with thermal boundaries. *Mon. Wea. Rev.*, **108**, 322–336, https://doi.org/10.1175/1520-0493(1980)108<0322:ASOTTI>2.0.CO;2.

——, D. Perkey, and J. Fritsch, 1981: Evolution of upper tropospheric features during the development of a mesoscale convective complex. *J. Atmos. Sci.*, **38**, 1664–1674, https://doi.org/10.1175/1520-0469(1981)038<1664:EOUTFD>2.0.CO;2.

Markowski, P., and Y. Richardson, 2006: On the classification of vertical wind shear as directional shear versus speed shear. *Wea. Forecasting*, **21**, 242–247, https://doi.org/10.1175/WAF897.1.

——, and ——, 2011: *Mesoscale Meteorology in Midlatitudes.* Wiley-Blackwell, 424 pp.

——, C. Hannon, J. Frame, E. Lancaster, A. Pietrycha, R. Edwards, and R. L. Thompson, 2003: Characteristics of vertical wind profiles near supercells obtained from the Rapid Update Cycle. *Wea. Forecasting*, **18**, 1262–1272, https://doi.org/10.1175/1520-0434(2003)018<1262:COVWPN>2.0.CO;2.

McCaul, E. W., and M. L. Weisman, 2001: The sensitivity of simulated supercell structure and intensity to variations in the shapes of environmental buoyancy and shear profiles. *Mon. Wea. Rev.*, **129**, 664–687, https://doi.org/10.1175/1520-0493(2001)129<0664:TSOSSS>2.0.CO;2.

Melhauser, C., and F. Zhang, 2012: Practical and intrinsic predictability of severe and convective weather at the mesoscales. *J. Atmos. Sci.*, **69**, 3350–3371, https://doi.org/10.1175/JAS-D-11-0315.1.

Nakanishi, M., and H. Niino, 2006: An improved Mellor-Yamada level-3 model: Its numerical stability and application to a

regional prediction of advection fog. *Bound.-Layer Meteor.*, **119**, 397–407, https://doi.org/10.1007/s10546-005-9030-8.

——, and ——, 2009: Development of an improved turbulence closure model for the atmospheric boundary layer. *J. Meteor. Soc. Japan*, **87**, 895–912, https://doi.org/10.2151/jmsj.87.895.

Nicholls, M. E., R. A. Pielke, and W. R. Cotton, 1991: Thermally forced gravity waves in an atmosphere at rest. *J. Atmos. Sci.*, **48**, 1869–1884, https://doi.org/10.1175/1520-0469(1991)048<1869:TFGWIA>2.0.CO;2.

Ninomiya, K., 1971: Mesoscale modification of synoptic situations from thunderstorm development as revealed by ATS III and aerological data. *J. Appl. Meteor.*, **10**, 1103–1121, https://doi.org/10.1175/1520-0450(1971)010<1103:MMOSSF>2.0.CO;2.

Olsson, P. Q., and W. R. Cotton, 1997: Balanced and unbalanced circulations in a primitive equation simulation of a midlatitude MCC. Part II: Analysis of balance. *J. Atmos. Sci.*, **54**, 479–497, https://doi.org/10.1175/1520-0469(1997)054<0479:BAUCIA>2.0.CO;2.

Phoenix, D. B., C. R. Homeyer, M. C. Barth, and S. B. Trier, 2019: Mechanisms responsible for stratosphere-to-troposphere transport around a mesoscale convective system anvil. *J. Geophys. Res. Atmos.*, **125**, e2019JD032016, https://doi.org/10.1029/2019JD032016.

Rasmussen, E. N., 2015: VORTEX-Southeast program overview. National Severe Storms Laboratory Rep., 36 pp.

——, 2003: Refined supercell and tornado forecast parameters. *Wea. Forecasting*, **18**, 530–535, https://doi.org/10.1175/1520-0434(2003)18<530:RSATFP>2.0.CO;2.

——, and D. O. Blanchard, 1998: A baseline climatology of sounding-derived supercell and tornado forecast parameters. *Wea. Forecasting*, **13**, 1148–1164, https://doi.org/10.1175/1520-0434(1998)013<1148:ABCOSD>2.0.CO;2.

Raymond, D., 1992: Nonlinear balance and potential-vorticity thinking at large Rossby number. *Quart. J. Roy. Meteor. Soc.*, **118**, 987–1015, https://doi.org/10.1002/qj.49711850708.

Riemer, M., S. C. Jones, and C. A. Davis, 2008: The impact of extratropical transition on the downstream flow: An idealized modelling study with a straight jet. *Quart. J. Roy. Meteor. Soc.*, **134**, 69–91, https://doi.org/10.1002/qj.189.

Roebber, P. J., D. M. Schultz, and R. Romero, 2002: Synoptic regulation of the 3 May 1999 tornado outbreak. *Wea. Forecasting*, **17**, 399–429, https://doi.org/10.1175/1520-0434(2002)017<0399:SROTMT>2.0.CO;2.

Rotunno, R., and J. B. Klemp, 1982: The influence of the shear-induced pressure gradient on thunderstorm motion. *Mon. Wea. Rev.*, **110**, 136–151, https://doi.org/10.1175/1520-0493(1982)110<0136:TIOTSI>2.0.CO;2.

——, and J. Klemp, 1985: On the rotation and propagation of simulated supercell thunderstorms. *J. Atmos. Sci.*, **42**, 271–292, https://doi.org/10.1175/1520-0469(1985)042<0271:OTRAPO>2.0.CO;2.

Rowe, S. M., and M. H. Hitchman, 2015: On the role of inertial instability in stratosphere–troposphere exchange near midlatitude cyclones. *J. Atmos. Sci.*, **72**, 2131–2151, https://doi.org/10.1175/JAS-D-14-0210.1.

——, and ——, 2016: On the relationship between inertial instability, poleward momentum surges, and jet intensifications near midlatitude cyclones. *J. Atmos. Sci.*, **73**, 2299–2315, https://doi.org/10.1175/JAS-D-15-0183.1.

Sherburn, K. D., M. D. Parker, J. R. King, and G. M. Lackmann, 2016: Composite environments of severe and nonsevere high-shear, low-CAPE convective events. *Wea. Forecasting*, **31**, 1899–1927, https://doi.org/10.1175/WAF-D-16-0086.1.

Skamarock, W. C., and Coauthors, 2008: A description of the Advanced Research WRF version 3. NCAR Tech. Note NCAR/TN-475+STR, 113 pp., https://doi.org/10.5065/D68S4MVH.

Steinfeld, D., and S. Pfahl, 2019: The role of latent heating in atmospheric blocking dynamics: A global climatology. *Climate Dyn.*, **53**, 6159–6180, https://doi.org/10.1007/s00382-019-04919-6.

Stensrud, D. J., 1996: Effects of persistent, midlatitude mesoscale regions of convection on the large-scale environment during the warm season. *J. Atmos. Sci.*, **53**, 3503–3527, https://doi.org/10.1175/1520-0469(1996)053<3503:EOPMMR>2.0.CO;2.

Stoelinga, M. T., 1996: A potential vorticity-based study of the role of diabatic heating and friction in a numerically simulated baroclinic cyclone. *Mon. Wea. Rev.*, **124**, 849–874, https://doi.org/10.1175/1520-0493(1996)124<0849:APVBSO>2.0.CO;2.

Thompson, G., R. M. Rasmussen, and K. Manning, 2004: Explicit forecasts of winter precipitation using an improved bulk microphysics scheme. Part I: Description and sensitivity analysis. *Mon. Wea. Rev.*, **132**, 519–542, https://doi.org/10.1175/1520-0493(2004)132<0519:EFOWPU>2.0.CO;2.

——, P. R. Field, R. M. Rasmussen, and W. D. Hall, 2008: Explicit forecasts of winter precipitation using an improved bulk microphysics scheme. Part II: Implementation of a new snow parameterization. *Mon. Wea. Rev.*, **136**, 5095–5115, https://doi.org/10.1175/2008MWR2387.1.

Thompson, R. L., and R. Edwards, 2000: An overview of environmental conditions and forecast implications of the 3 May 1999 tornado outbreak. *Wea. Forecasting*, **15**, 682–699, https://doi.org/10.1175/1520-0434(2000)015<0682:AOOECA>2.0.CO;2.

——, ——, J. A. Hart, K. L. Elmore, and P. Markowski, 2003: Close proximity soundings within supercell environments obtained from the Rapid Update Cycle. *Wea. Forecasting*, **18**, 1243–1261, https://doi.org/10.1175/1520-0434(2003)018<1243:CPSWSE>2.0.CO;2.

Thorncroft, C., B. Hoskins, and M. McIntyre, 1993: Two paradigms of baroclinic-wave life-cycle behaviour. *Quart. J. Roy. Meteor. Soc.*, **119**, 17–55, https://doi.org/10.1002/qj.49711950903.

Trapp, R. J., 2014: On the significance of multiple consecutive days of tornado activity. *Mon. Wea. Rev.*, **142**, 1452–1459, https://doi.org/10.1175/MWR-D-13-00347.1.

Uccellini, L. W., and D. R. Johnson, 1979: The coupling of upper and lower tropospheric jet streaks and implications for the development of severe convective storms. *Mon. Wea. Rev.*, **107**, 682–703, https://doi.org/10.1175/1520-0493(1979)107<0682:TCOUAL>2.0.CO;2.

——, and S. E. Koch, 1987: The synoptic setting and possible energy sources for mesoscale wave disturbances. *Mon. Wea. Rev.*, **115**, 721–729, https://doi.org/10.1175/1520-0493(1987)115<0721:TSSAPE>2.0.CO;2.

——, P. J. Kocin, R. A. Petersen, C. H. Wash, and K. F. Brill, 1984: The Presidents' Day cyclone of 18–19 February 1979: Synoptic overview and analysis of the subtropical jet streak influencing the pre-cyclogenetic period. *Mon. Wea. Rev.*, **112**, 31–55, https://doi.org/10.1175/1520-0493(1984)112<0031:TPDCOF>2.0.CO;2.

Van Tuyl, A. H., and J. A. Young, 1982: Numerical simulation of nonlinear jet streak adjustment. *Mon. Wea. Rev.*, **110**, 2038–2054, https://doi.org/10.1175/1520-0493(1982)110<2038:NSONJS>2.0.CO;2.

Weisman, M. L., and J. B. Klemp, 1984: The structure and classification of numerically simulated convective storms in directionally

varying wind shears. *Mon. Wea. Rev.*, **112**, 2479–2498, https://doi.org/10.1175/1520-0493(1984)112<2479:TSACON>2.0.CO;2.

——, and R. Rotunno, 2000: The use of vertical wind shear versus helicity in interpreting supercell dynamics. *J. Atmos. Sci.*, **57**, 1452–1472, https://doi.org/10.1175/1520-0469(2000)057<1452:TUOVWS>2.0.CO;2.

——, and Coauthors, 2015: The Mesoscale Predictability Experiment (MPEX). *Bull. Amer. Meteor. Soc.*, **96**, 2127–2149, https://doi.org/10.1175/BAMS-D-13-00281.1.

Wernli, H., S. Dirren, M. A. Liniger, and M. Zillig, 2002: Dynamical aspects of the life cycle of the winter storm 'Lothar' (24–26 December 1999). *Quart. J. Roy. Meteor. Soc.*, **128**, 405–429, https://doi.org/10.1256/003590002321042036.

Wetzel, P. J., W. R. Cotton, and R. L. McAnelly, 1983: A long-lived mesoscale convective complex. Part II: Evolution and structure of the mature complex. *Mon. Wea. Rev.*, **111**, 1919–1937, https://doi.org/10.1175/1520-0493(1983)111<1919:ALLMCC>2.0.CO;2.

Whitaker, J. S., and C. A. Davis, 1994: Cyclogenesis in a saturated environment. *J. Atmos. Sci.*, **51**, 889–908, https://doi.org/10.1175/1520-0469(1994)051<0889:CIASE>2.0.CO;2.

Winters, A. C., D. Keyser, L. F. Bosart, and J. E. Martin, 2020: Composite synoptic-scale environments conducive to North American polar–subtropical jet superposition events. *Mon. Wea. Rev.*, **148**, 1987–2008, https://doi.org/10.1175/MWR-D-19-0353.1.

Wolf, B. J., and D. R. Johnson, 1995: The mesoscale forcing of a midlatitude upper-tropospheric jet streak by a simulated convective system. Part I: Mass circulation and ageostrophic processes. *Mon. Wea. Rev.*, **123**, 1059–1087, https://doi.org/10.1175/1520-0493(1995)123<1059:TMFOAM>2.0.CO;2.

Zack, J. W., and M. L. Kaplan, 1987: Numerical simulations of the subsynoptic features associated with the AVE-SESAME I case. Part I: The preconvective environment. *Mon. Wea. Rev.*, **115**, 2367–2394, https://doi.org/10.1175/1520-0493(1987)115<2367:NSOTSF>2.0.CO;2.

Zhang, C., Y. Wang, and K. Hamilton, 2011: Improved representation of boundary layer clouds over the southeast Pacific in ARW-WRF using a modified Tiedtke cumulus parameterization scheme. *Mon. Wea. Rev.*, **139**, 3489–3513, https://doi.org/10.1175/MWR-D-10-05091.1.

Zhang, D.-L., and R. Harvey, 1995: Enhancement of extratropical cyclogenesis by a mesoscale convective system. *J. Atmos. Sci.*, **52**, 1107–1127, https://doi.org/10.1175/1520-0469(1995)052<1107:EOECBA>2.0.CO;2.

Zhang, F., S. E. Koch, C. A. Davis, and M. L. Kaplan, 2000: A survey of unbalanced flow diagnostics and their application. *Adv. Atmos. Sci.*, **17**, 165–183, https://doi.org/10.1007/s00376-000-0001-1.

——, N. Bei, R. Rotunno, C. Snyder, and C. C. Epifanio, 2007: Mesoscale predictability of moist baroclinic waves: Convection-permitting experiments and multistage error growth dynamics. *J. Atmos. Sci.*, **64**, 3579–3594, https://doi.org/10.1175/JAS4028.1.